

# The CLAS12 High Threshold Cherenkov Counter

Y.G. Sharabian<sup>a</sup>, V.D. Burkert<sup>a</sup>, A. Biselli<sup>b</sup>, R. Badui<sup>m</sup>, S. Christo<sup>a</sup>, C. Cuevas<sup>a</sup>, H. Dong<sup>a</sup>, S. Danagoulian<sup>c</sup>, A. Ellis<sup>a</sup>, L. Elouadrhiri<sup>a</sup>, B. Eng<sup>a</sup>, K. Hafidi<sup>d</sup>, I. Illari<sup>e</sup>, G. Jacobs<sup>a</sup>, J. Joo<sup>f</sup>, K. Joo<sup>f</sup>, D. Kashy<sup>a</sup>, A.V. Kubarovsky<sup>f</sup>, V.P. Kubarovsky<sup>a</sup>, S. Maiylian<sup>g</sup>, N. Markov<sup>a</sup>, M. McClellan<sup>f</sup>, M. McMullen<sup>a</sup>, B. Miller<sup>a</sup>, S. Miller-Smith<sup>k</sup>, D. Nickolas<sup>k</sup>, R. Niyazov<sup>h</sup>, R. Paremuzyan<sup>i</sup>, W. Phelps<sup>j</sup>, V. Popov<sup>a</sup>, J. Price<sup>k</sup>, A. Puckett<sup>f</sup>, B. Raydo<sup>a</sup>, D. Riser<sup>f</sup>, P. Stoler<sup>h</sup>, A. Vlassov<sup>l</sup>, A. Voskanyan<sup>g</sup>

<sup>a</sup>Thomas Jefferson National Accelerator Facility, Newport News, VA 23606

<sup>b</sup>Fairfield University, Fairfield, CT 06824

<sup>c</sup>North Carolina Agricultural and Technical State University, Greensboro, NC 27401

<sup>d</sup>Argonne National Laboratory, Argonne, IL 60439

<sup>e</sup>The George Washington University, Washington, DC 20052

<sup>f</sup>University of Connecticut, Storrs, CT 06269

<sup>g</sup>Yerevan Physics Institute, 375036, Yerevan, Armenia

<sup>h</sup>Rensselaer Polytechnic Institute, Troy, NY 12180

<sup>i</sup>University of New Hampshire, Durham, NH 03834

<sup>j</sup>Christopher Newport University, Newport News, VA 23606

<sup>k</sup>California State University, Dominguez Hills, Carson, CA 90747

<sup>l</sup>National Research Centre Kurchatov Institute - ITEP, Moscow, 117218, Russia

<sup>m</sup>Florida International University, Miami, FL 33199

---

## Abstract

The High Threshold Cherenkov Counter (HTCC) is one of the detector systems of the CLAS12 spectrometer, and is used to generate a fast trigger signal in electron scattering experiments in the polar angle range from  $5^\circ$  to  $35^\circ$ . The HTCC is installed in front of the drift chambers and introduces a minimal amount of additional material within the acceptance. The HTCC is one unit whose core component is a multifocal mirror that consists of 60 lightweight ellipsoidal mirrors. It is important that the HTCC provides efficient coverage of the CLAS12 forward acceptance with no gaps. In order to achieve this, each sector of the CLAS12 Forward Detector is covered by 2 identical half-sector mirrors that focus Cherenkov light on 8 phototubes. The HTCC has a total of 48 channels with Electron Tubes 9823QKB photomultipliers that have a 5-in quartz face plate to detect Cherenkov light. The system provides rejection of charged  $\pi$ -mesons with momenta below 4.8 GeV for the reliable identification of scattered electrons. In this paper the details of the design, construction, calibration, and performance results of the HTCC are presented.

---

## 1. Overview

The CLAS12 spectrometer in Hall B at Jefferson Laboratory (JLab) has been designed and built for comprehensive experimental studies of matter, using primarily a high-energy electron beam [1]. For these experiments this spectrometer must be capable of detecting scattered electrons within the entirety of its forward acceptance range and at the highest possible efficiency with low background. The High Threshold Cherenkov Counter (HTCC) (see Fig. 1) of CLAS12 was designed and built to fulfill the goal of detecting scattered electrons in the range of polar angles from  $5^\circ$  to  $35^\circ$  in conjunction

with other detector systems of the CLAS12 Forward Detector and to generate a fast trigger signal for event readout.

The distinguishing features of the detector were influenced by its location in front of the drift chambers (DC) [2], which required that the HTCC incorporate a minimum amount of material in the active area in front of the tracking detectors. Because the HTCC is a single module system, it occupies very limited space within CLAS12. Consequently, the construction requirements (including transportation to the hall and installation into the nominal location of the detector) were important for its structural design.



Fig. 1: Fully assembled High Threshold Cherenkov Counter.

## 2. Requirements

The core requirements for the HTCC are summarized in Table 1. Based on these necessary general conditions, we derived the more specific and essential demands that had to be taken into consideration. As a result, it was necessary to spend time on the research and development (R&D) of scaled prototype mirror facets. In order to provide minimal losses in light collection, i.e. to provide maximal signal strength, an ellipsoidal multifocal mirror design was chosen. This necessitated a significant upgrade of the available machines for manufacturing the parts. Thus the formulated R&D goals covered both the properties of the mirrors and the equally important choice of construction technology. It must be mentioned that any polishing of working surfaces was excluded from consideration in the first place due to the very high cost and time-consuming procedures that would have been involved otherwise.

With regard to the combined mirror installation, it was critical to avoid the use of any mirror support structure within the acceptance of the HTCC. One of the problems that was addressed was finding a way to assemble the mirror to make it a self-supporting, lightweight structure. In this case the mirror design did not allow for adjustment of individual mirror facets after the combined mirror was fully assembled. Thus the construction and assem-

bly procedures had to be precise enough to guarantee the geometrical specifications of the multifocal mirror, which could then be adjusted only as a whole unit.

Directly assembling the detector in the experimental hall was impractical for several reasons. It would require having a controlled clean environment in the area. Additionally, since the HTCC is a single unit detector that covers all six sectors of the CLAS12 Forward Detector, its size was larger than the space available for assembly.

Environmental concerns were also addressed: such as what gases would be in use, the inside/outside temperature of the detector, the humidity of the air, as well as the quality of the pavement along the transportation route. Additional requirements with regard to the detector maintenance and year-round controls were applied to the HTCC by using experience acquired with the Low Threshold Cherenkov Counter built for CLAS [3].

## 3. Hardware Components and Construction

### 3.1. Lightweight Mirror Prototype Construction

The multifocal ellipsoidal mirror is the most critical component of the detector. A comprehensive R&D program was conducted for the purpose of addressing all of the key requirements and to find possible solutions, and to test and verify the entire technological chain of building mirror prototypes on a 1:2 scale. All core parameters of the detector were checked and/or derived from the results of Monte Carlo (MC) simulations.

Because there is no mirror support structure, no additional material is introduced within the acceptance, i.e. in front of the drift chambers. Therefore the major requirement we needed to satisfy was to build a lightweight and self-supporting multifocal mirror consisting of many ellipsoidal mirror facets glued together along their edges. This led to several problems to solve. One of them was to define the contact surfaces of adjacent mirror facets that would allow final assembly to be completed without any shape adjustments that would leave no gaps between them. An analytic solution of a system of two second-order equations that describe two intersecting ellipsoidal surfaces leads to an equation of fourth order in general form. The solutions for any two intersecting ellipsoidal mirrors of different parameters have been used directly in the design: the line along which two ellipsoidal surfaces intersect

Table 1: Core requirements for the HTCC design.

PARAMETER	DESIGN VALUE
Working Gas	CO <sub>2</sub> @ 1 atm, 25°C
Angular Coverage	$\theta = 5^\circ - 35^\circ$ ; $\phi = 0^\circ - 360^\circ$
Threshold	15 MeV (electrons)
Threshold	4.9 GeV (charged pions)
Rejection of charged pions	$0.5 \times 10^3$ ( $\sim 99\%$ electron detection efficiency)
Overall Dimensions	$\geq 15$ ft and $L = 6$ ft along beam direction
Mirror Type	Combined, self-supporting
Mirror Substrate Structure	Composite
Mirror Thickness	200 mg/cm <sup>2</sup>
Number of Channels	$(12 \times 4) = 48$
Photomultiplier Tubes	Photocathode of $\sim 5$ in diameter
Number of Reflections	1 (in most cases)
Environment	Magnetic field of 35 G (along PMT axis)

is a flat line of second order, i.e. that which entirely belongs to one particular well-defined plane. This plane coincides with the edge of each of two adjacent facets that had to be glued together.

110 One of the R&D goals was to test this possible solution by building three scaled prototype ellipsoidal facets that formed a portion of the combined mirror. A complete set of tooling necessary for the thermal shaping of the front and back films, manufacturing of the ellipsoidal substrates, assembly of the facets, and final trimming were successfully designed, constructed, and tested. Some parts for tests are shown in Fig. 2.

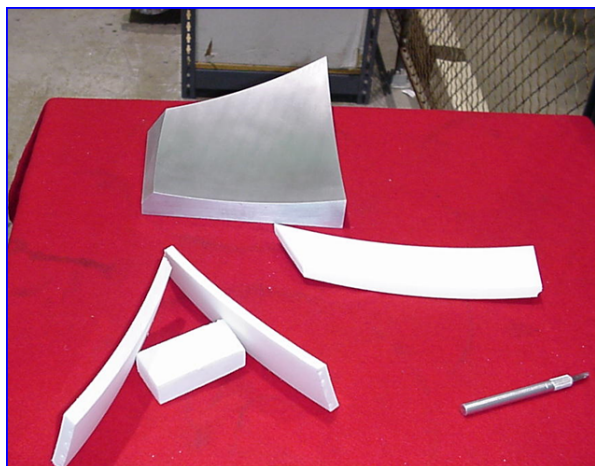


Fig. 2: Three prototype ellipsoidal foam mirror facets (bottom) and the spherical master table (top).

120 Three prototype facets (no reflective coatings on the substrates) were put together, touching each

other exactly as designed on the spherical working surface of the assembly table. The back of each facet was of the same spherical shape. The facets were left under their own weight on the master table of the spherical working surface for several months, (see Fig. 3), to allow checking for any changes in shape and/or quality.

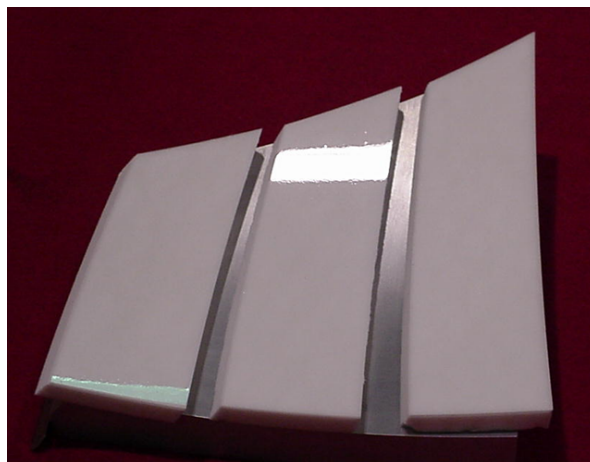


Fig. 3: Three prototype ellipsoidal mirror facets on the spherical master table. They were placed so that they would not touch each other. This was in order to leave them free and to check their shape stability.

We learned the following lessons:

- Each substrate must have a multi-layer structure to avoid post-assembly deformations due to glue shrinkage;
- The thickness of the substrate material had to

be between  $3/8$  in and  $3/4$  in to satisfy the requirements and to stay rigid enough;

- 135 • The substrate material ROHACELL polymethacrylimide foam with a density up to  $150 \text{ mg/cm}^2$  could be employed since it has uniform mechanical properties and high radiation resistance;
- 140 • The trimming technology had to be improved to provide increased precision of the mechanical processing and final assembly;
- 145 • In all gluing operations non-shrinking glues had to be used or a special technique had to be developed to avoid post-polymerization effects;
- 150 • Acrylic films of optical quality have to be used for the front and back surfaces of the mirrors to avoid hand-polishing;
- 155 • It is critical that there is structural stability of the mirror facets during the gluing process, which includes the complete polymerization time to avoid changes of the geometry of the components.

The results obtained were useful in building the final multifocal mirror. Figure 4 shows one of the ellipsoidal facets being prepared for the combined mirror assembly. Final assembly of a  $1/12$  portion of the full mirror, consisting of five ellipsoidal coated mirror facets or one “half-sector”, is shown in Fig. 5.

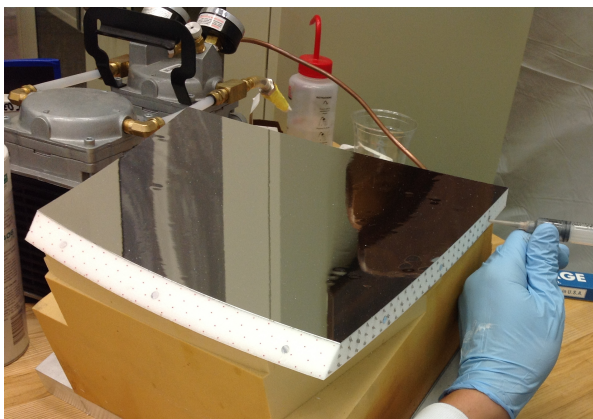


Fig. 4: An ellipsoidal mirror facet with all four flat contact surfaces prepared for gluing.

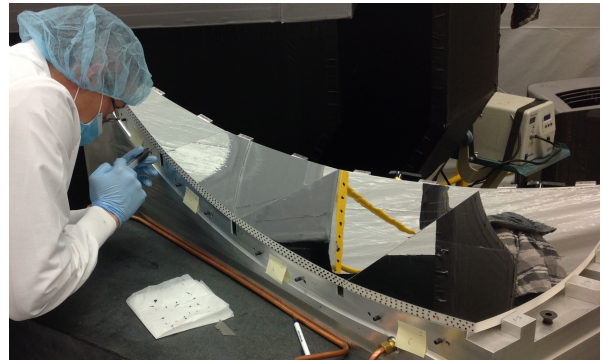


Fig. 5: Five ellipsoidal mirror facets glued together make up  $1/12$  of the full HTCC mirror (half of a CLAS12 forward sector).

### 3.2. Ellipsoidal Mirror Facet Manufacturing

The usage of high-accuracy mechanical processing was absolutely unavoidable in providing the high-precision mirror facets for the final combined mirror. Putting together 60 ellipsoidal facets of semi-trapezoidal shape, fitting against each other without adjustment of the overall dimensions of the adjacent facet seams, is a difficult task. In order to adjust the facets of the combined mirror, each individual facet would need to have its own support infrastructure, and this would unavoidably introduce additional material. With these concerns in mind, all of the mechanical processing of the mirror facets was performed with a HAAS 5-axis milling machine. This allowed us to develop and use special trimming technology for the facets. One such technique was the “one-shot” method, which provided the ability from one setting to trim any facet with 3 or 4 contact surfaces that needed to be glued. This was done to exclude, or at least minimize, the errors introduced when we reset the orientation of the facets while we cut 3 or 4 edge planes under different combinations of angles. We estimated that any deviation in the designed dimensions of more than about  $0.005$  in would make the combined, precision assembly of so many mirror substrates impossible. This was because any post-manufacturing adjustment of any of mirror substrates was not an option. In no way could two facets be found to be either overlapping or with significant gaps between them. These gaps could be as wide as the thickness of a regular glue joint obtained by simple contact pressure. Otherwise, if these gaps were any larger, they would reduce the working acceptance and lead to reduced detector efficiency.

The polishing process of large mirrors (8-9 ft diameter) usually means that the manufacturing process is both labor intensive and time consuming, thus leading it to be very expensive. Therefore, we looked for solutions to completely avoid any polishing. Due to the fact that we did not require sharp images, the mirror facets were thus constructed to only work as efficient light collectors. To accomplish the goal we developed and established an entire assembly procedure, followed by tests of the construction and rating of the final results.

Another issue we addressed was the choice between gluing or mechanical plug-pin assembly procedures. Clearly gluing introduces deformations due to the shrinkage of any glue. On the other hand, an assembly procedure that uses location pins results in a more complicated joint since it requires the high-precision processing of plastic foam parts that are both very lightweight and mechanically weak. Moreover, if any joint deformation was observed after the first assembly attempt, then many of the parts involved (including the mirror facets) could not be re-manufactured or used again.

We built 12 identical half-sectors of the combined mirror. Each half-sector consists of 4 ellipsoidal mirrors of different parameters. The outermost mirror was too large to trim due to the limited travel of the milling machine table. Therefore, this particular mirror was made of two substrates that were a mirror image of each other. Consequently each half-sector includes 5 mirror substrates and the full HTCC mirror consists of 60 ellipsoidal mirror facets in total.

All mirror facets have the same composite (sandwich) structure: acrylic film (thickness 0.010 in) + foam (thickness 0.600 in) + acrylic film (thickness 0.010 in). The mirror substrate was made from ROHACELL PMI (polymethacrylimide) foam and the acrylic films were of optical quality. Manufacturing any substrate was a multi-stage process:

- Thermal shaping of the acrylic film shells for the front (ellipsoidal) and back (spherical) of the mirror;
- Manufacturing of the foam substrates;
- Assembly (gluing) of the sandwiched mirror substrate;
- Trimming of the sandwiched mirror substrate;
- Coating of the ellipsoidal faces of the substrate;

- Reflectivity tests of the mirror substrate.

Correspondingly we used 5 different high-precision, custom-made tooling sets for the thermal shaping, gluing, and trimming of the substrates. The thermal shaping was done in a low temperature Precision oven with better than  $0.5^{\circ}\text{C}$  temperature uniformity in the volume. The tooling set for the manufacturing of mirror facet #3, which covers the polar angle in range  $\theta = 12.5^{\circ} - 20^{\circ}$  and the azimuthal angular interval of  $\Delta\phi = 30^{\circ}$ , is shown in Fig. 6.



Fig. 6: Tooling set for the manufacture of mirror facet #3.

The scheme of shaping the acrylic shells is illustrated in Fig. 7. The shaping process was done at temperatures of  $105^{\circ}\text{C}$  and differential pressures below 1 atm. There were two possibilities to shape the shells: use vacuum shaping or just pressurizing the volume up to 2-3 psi differential. Both options were tried. The option of pressurizing the volume was chosen and used: it provided better control on the process, i.e. better results. Since the tooling parts were heavy and therefore required a relatively long time to reach the required temperature, the operations with the oven would take about 3-4 hours, and the whole process of shaping one shell (load the tooling, heat it up in the oven, cool down to room temperature, and unload the tooling) would take up to 5 hours.

The loaded tooling set for shaping the front ellipsoidal shell in the oven by pressurizing the volume above the film is shown in Fig. 8. Figure 9 shows the shaped acrylic shell for the front of the mirror.

The cut-out of the foam substrate and processing of the back surface of spherical shape was performed without using any custom-made tools.

The front ellipsoidal surface was cut using the tooling that was also used for the final trimming of

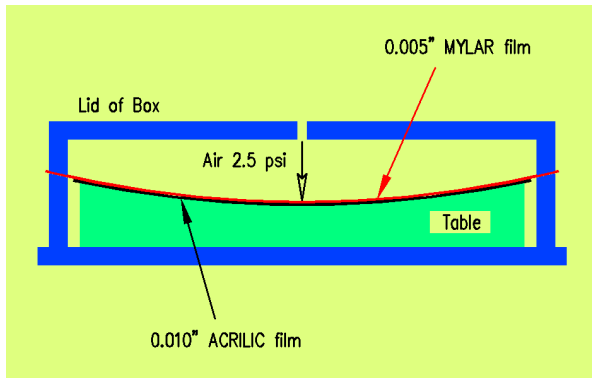


Fig. 7: Scheme of thermal shaping of the spherical shell for the back of the mirrors.

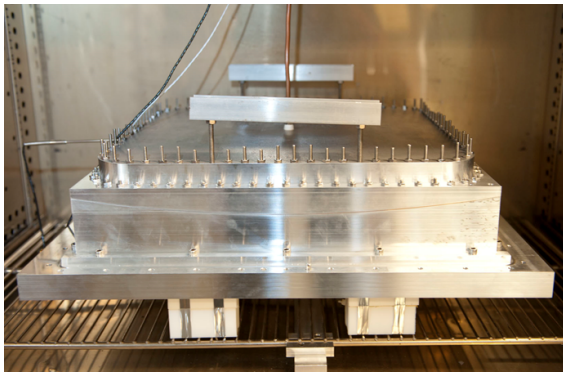


Fig. 8: Loaded tooling set for shaping the front ellipsoidal shell of mirror facet #3 in the oven by pressurizing the volume with dry air using 1/4-in copper tubing.

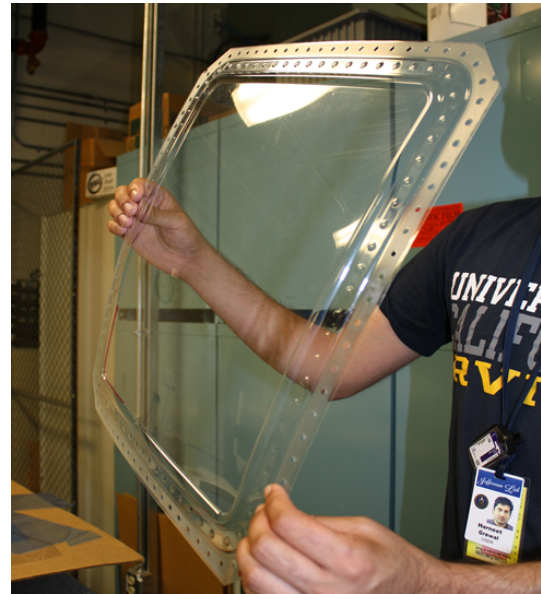


Fig. 9: Thermally shaped front ellipsoidal shell for mirror facet #3.

280 the sandwiched glued facet. Once the front surface  
 was cut, the facet was taken off the tooling set for  
 the next operation of gluing the acryl-foam-acryl  
 sandwich. Figure 10 shows the fully processed foam  
 285 substrate for mirror facet #3 ready for the assembly  
 of the sandwich. The scheme for the assembly of the  
 sandwiched substrate is shown in Fig. 11. In Fig. 12  
 the fully assembled sandwiched substrate for mirror  
 facet #3 ready for the final trimming is shown.

290 After gluing of the sandwich, it was put back in  
 the tooling set for the final precision trimming. The  
 shells were designed and processed in a way that  
 allowed unequivocal and simple alignment of all parts  
 during assembly. Each tooling set had well-defined  
 295 reference points to provide precise orientation of the  
 set during processing of the parts. Additionally, the  
 relative position of all tooling components was  
 defined by location pins. Using the same set of tooling  
 for cutting the face and trimming the facet, guar-  
 anteed automatic perfect relative alignment of the

300 parts being glued together.

Before the trimming operation, the front work-  
 ing face of the substrate was covered with a special  
 tight-fitting protective film to prevent damage or  
 pollution of the working surface while trimming the  
 305 substrate. For better control of the uniformity of  
 glue application (thickness, formation of unwanted  
 bubbles), the first manufactured mirror facet was  
 assembled using epoxy glue with black dye. The  
 trimming was done in two steps. In order to avoid  
 the front shell peeling off the foam, the substrate  
 was cut through the front shell only using a very  
 small diameter (0.006 in) end mill, see Fig. 13.  
 Then the outer portion of the shell was safely peeled  
 off the substrate and the remaining trimming was  
 performed using a long end mill. The completed  
 final trimming of the facet is shown in Fig. 14.

During final milling the substrate was secured in  
 place by inserting soft foam wedges along the par-  
 tially cut sides and glued to the outer portion of the  
 320 substrate being trimmed. This completely elimi-  
 nated any vibration that could ruin the accuracy of  
 the processing. Figure 15 shows the completed mir-  
 ror facet #3 ready for deposition of the reflective  
 coating. All substrate trimming was done without  
 any re-positioning of the facet during the procedure.

The face of the mirror substrate did not require  
 any processing before deposition of the reflector ma-  
 terial. The total thickness of the mirror is 130-



Fig. 10: A completed foam substrate that forms the core of the mirror facet.



Fig. 12: Sandwiched mirror facet after gluing components as shown in Fig. 11.

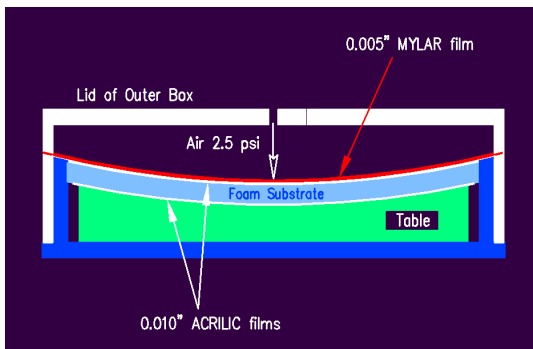


Fig. 11: Scheme for gluing of the sandwiched mirror substrate.

135 mg/cm<sup>2</sup>. Acrylic films were glued to both sides of the substrates to compensate deformation introduced by the shrinking of the thin epoxy glue layers. No shrinkage effects in any of the produced substrates was observed, thus long-term problems with mirror shape were completely eliminated. All critical mirror fabrication steps were performed in a clean room (Class 1000). In addition, for better results, all parts were individually cleaned using an ionizing gun right before assembly. As well, the clean room included a clean bench with a HEPA air filter next to the assembly table that blew filtered air over the table. Thermal and mechanical processing was done either with protection films covering critical surfaces or encapsulated in a gas-tight volume to prevent dust or any other unwanted depositions from damaging the working surface or

otherwise compromising the mirror reflectance.

### 3.3. Tests of Mirrors Coated with Reflective Material

Evaporated Coatings Incorporated (ECI) was chosen from among four potential vendor companies to perform vacuum deposition of the reflective coating onto the HTCC mirror substrates. Test samples (flat sheets of acrylic, one untouched and one subjected to the same thermal-shaping process used to form the front and back surfaces of the mirrors) coated by ECI were the most reflective over the entire wavelength range of interest.

For the sample reflectivity tests, a 30 W deuterium lamp was used as an ultraviolet (UV) source from 200-400 nm, and a 50 W quartz-tungsten halogen (QTH) lamp was used as a source of visible light from 370-650 nm. A monochromatic test beam for the reflectivity measurements was generated by a Newport model 74125 computer-controlled monochromator. A Newport model 10Z40A1.2 flat broadband mirror was used as a repeatable reference standard for the reflectance measurements. The mirror consists of a UV-enhanced aluminum coating on a 1/4-in thick, 1-in diameter Zerodur substrate, with a protective overcoat of UV-transparent magnesium fluoride to prevent oxidation.

The custom coating material used by ECI has an acceptable reflection coefficient in the UV-range

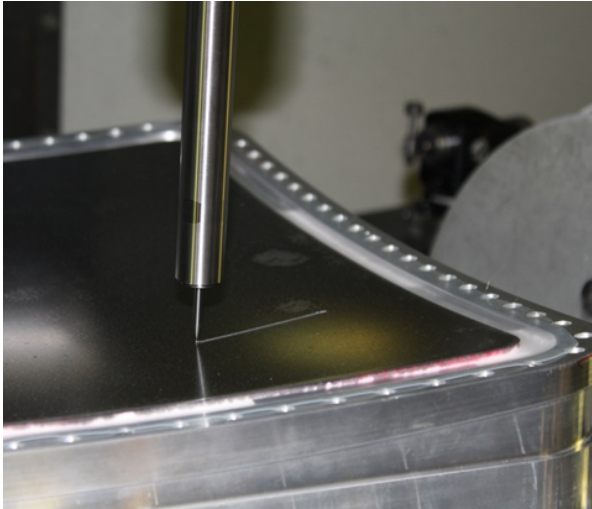


Fig. 13: Cutting through the acrylic shell of the substrate using a small diameter end mill.

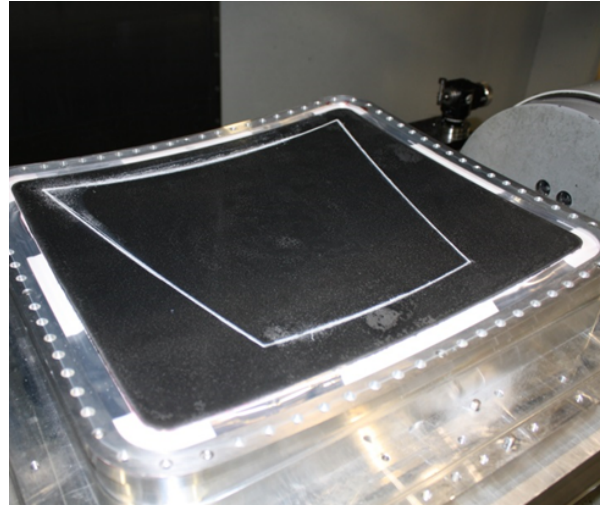


Fig. 14: Completed final trimming of mirror facet #3.

and is resistant to oxidation at room temperatures. Each mirror facet was coated individually along with small flat acryl sample. The coated acryl sample facet then was tested at the company. The final quality control measurements of the coated mirror facets was done at Jefferson Lab. Figure 16 shows typical results of the reflectance measurements of an ellipsoidal mirror facet for the HTCC. The measured reflectance of the mirror facet (black dots) is very close to the specification shown by the dashed curve. The reflectance of the reference flat 1-in diameter mirror specified by the vendor and checked at Jefferson Lab is shown in Fig. 17. The measurement technique has small systematic uncertainties of about 1-2%.

### 3.4. Assembly and Tests of Half-Sector Mirrors

The assembly of the half-sector mirrors was performed on the high-precision half-sector assembly table. The assembly procedure had to ensure that there were no overlaps or gaps between half-sectors. Figure 18 shows the table used for the assembly of all 12 half-sector mirrors. The table was made of solid aluminum alloy block and has several features important for assembly with the required accuracy:

- The overall dimensions of the working surface defined the overall dimensions of the half-sector mirror being assembled;
- The table was equipped with side plates on the left and right of each facet (8 plates total);

- The table was designed to be used for gluing of the facets to each other;
- The radial and transverse positions of the mirror could be controlled with an accuracy up to 0.001 in by inserting spacers between the mirror facets and the side plates;
- Each of the 5 places for mounting the different mirror substrates functioned as a vacuum table with a spherical work surface, so that each facet used in the assembly could be put on the table and secured in place as needed by turning on the corresponding diaphragm vacuum pump;
- Along the edges of the adjacent mirrors that are in contact, the table has milled-out groves for collecting excess epoxy to prevent gluing of the facet to the table surface;
- Polymerization of the epoxy glue was possible to perform in a temperature and humidity-controlled environment;
- The table was part of the setup that allowed for geometry tests of the assembled half-sector.

The assembly of the combined mirror using location pins is preferable compared with side-to side direct gluing as there are no deformations involved due to unavoidable epoxy glue shrinkage. Nevertheless, it was decided not to use location pins since the thickness of the substrates (0.6 in) was relatively small and the mechanical strength of the

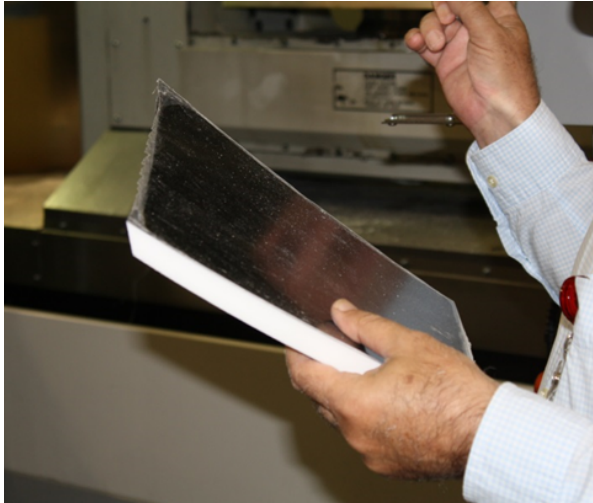


Fig. 15: Completely trimmed mirror facet #3 covered with protection film.

PMI foam that we used would introduce risks during final assembly, handling, and installation of the HTCC mirror. Therefore we decided to directly glue the facets to each other. The gluing technique was based on applying the glue in the form of dots uniformly distributed over the entire contact surface. The amount of glue in the dots and the distance between them were such that the glue spots compressed between the facets did not touch each other. In this case deformations caused by shrinkage of individual dots cancel each other and the shape of the final product stays unchanged. The only dots that introduce uncompensated shrinkage deformation are near the edges of the glued surfaces. The corresponding deformations do not change the mirror shape but they introduce a slight residual waviness of the edges of the mirrors with a pattern that repeats as the pattern of dots. In fact the only concern was to make sure the glue joints were strong enough. We ran comprehensive tests to come up with an acceptable solution for using this kind of joint. We tried several different patterns of glue application, amount and viscosity of the glue, applying glue on one side or both sides, etc. Figure 19 shows two identical foam pieces and the epoxy application pattern used in the tests of the glue joint.

Standard Hysol epoxy with black pigment and 1:1 silica filler to epoxy by volume was applied as small dots (0.08 in diameter). The viscosity of the epoxy filler mix was so thick that the glue did not bleed into the foam.

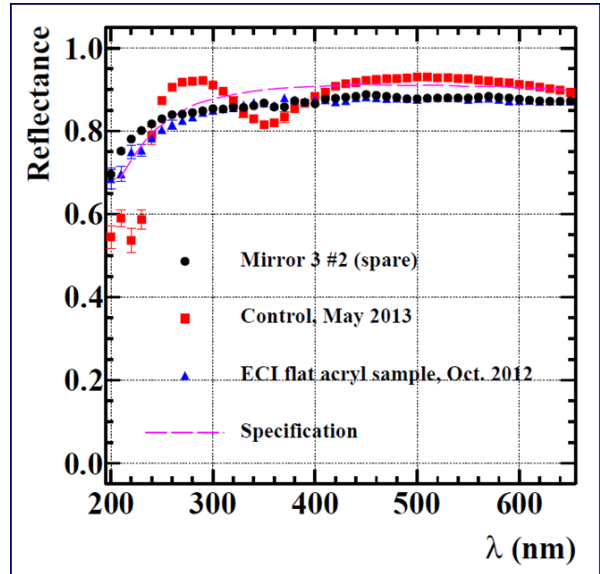


Fig. 16: Typical reflectivity of an ellipsoidal HTCC mirror facet as measured at JLab.

Figure 20 shows the test setup to check the strength of the glue joint using two sample substrate pieces. The epoxy cured for 72 hrs. The total force to break the glue joint was about 62 ft-lbs. The force was applied evenly and the foam was torn from the glue on both test pieces, see Fig. 21. The foam failed and not the glue itself. A set 0.004-in wide gap was left between the parts when gluing, and the glue was directly applied to one piece only. When the bond failed it pulled out almost all of the glued dots evenly except for the two places where the shims were set. The foam piece in Fig. 21 that has the dots on it was the same piece to which the epoxy was applied.

The assembly of half-sectors was done step-by-step by placing mirror facets on the table starting from the smallest mirror. The first facet once placed on the table was aligned and then checked for fit. After that the vacuum pump was turned on to secure the mirror. It was impossible to shift the facet on the table by even a little bit without deforming the mirror once the vacuum was established. The next step was to position the adjacent mirror with epoxy glue dots on it into position in contact with the first mirror. Once aligned it was independently secured on the table using the same vacuum pump. Epoxy glue dots were applied on the next facet and the procedure was repeated until the half-sector was fully assembled. Figure 22

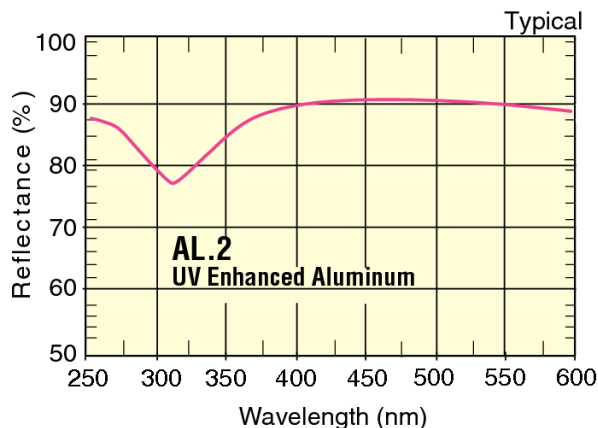


Fig. 17: Typical mirror reference reflectivity as specified by Newport.



Fig. 18: High-precision table for the assembly of the half-sector mirrors.

shows a partially assembled half-sector mirror. The right half (installed) and left half (yet missing) of the largest mirror have exactly the same geometry.

Figure 23 shows a fully assembled half-sector mirror. It was left on the table under pressure with vacuum pumps on for at least 24 hours or more depending on the polymerization results of the control glued samples.

The high-precision table was part of the half-sector mirror geometry test setup that was equipped with a low-energy red laser, gimbal-mounted in the target position, and with four focal planes. The relative locations of the laser, assembly table, and focal planes were strictly defined by the designed geometry of the HTCC light collection. The setup allowed for checking the actual geometry of light collection by each mirror using a point-like laser beam, as well as a beam rastered in the plane crossing any mirror over its entire surface. The light collection geometry was checked on



Fig. 19: Foam pieces marked for an approximately 22.5% epoxy coverage pattern.

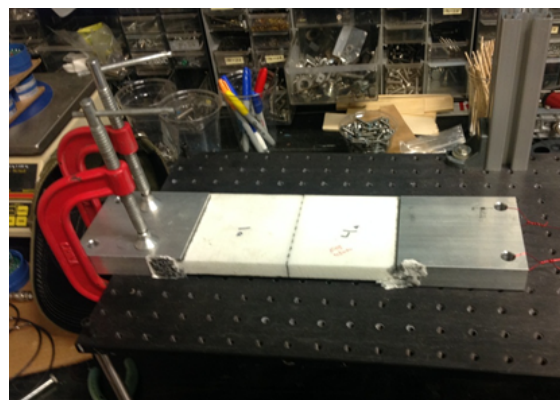


Fig. 20: Test setup to check the strength of the substrate glue joint.

the half-sector mirrors after complete polymerization of the glue. The pattern of the light collection obtained on the focal plane of the smallest mirror facet that covers polar and azimuthal angles of the scattering electrons in the range of  $\theta = 5^\circ - 12.5^\circ$  and  $\phi = 0^\circ - 30^\circ$  is shown in Fig. 24. The concentric circles on the focal plane are of diameter 1, 2, and 3 inches. Similar results have been obtained for the remaining three mirror facets covering polar angle ranges of  $\theta = 12.5^\circ - 20^\circ$ ,  $\theta = 20^\circ - 27.5^\circ$ , and  $\theta = 27.5^\circ - 35^\circ$ . The azimuthal angular coverage is the same for all facets. Figure 25 shows the light collection pattern for the outermost, largest mirror facet. All 12 half-sector mirrors were assembled following exactly the same procedures that al-



Fig. 21: Broken epoxy glue joint between two PMI foam pieces.

lowed us to closely control the overall dimensions and therefore the size of the gaps between adjacent half-sectors.

### 3.5. Assembly of the Combined Mirror

The combined HTCC mirror was assembled based on the experience acquired during the final assembly of the half-sector mirrors. In order to do this we designed and built the half-sector mirror vacuum holding table for assembly of the combined mirror. The design of this table and the accuracy of its manufacturing and construction were critical in providing the required parameters of the combined mirror, such as the geometry of the mirror optics, the stability of its shape, and its mechanical integrity. A peculiar feature of the combined HTCC mirror is that it had to provide the correct light collection geometry for all 60 of its mirror facets glued together. The option of making even very small adjustments of individual facets was excluded by the



Fig. 22: Partially assembled half-sector mirror. The left facet of the last largest mirror is not installed yet.

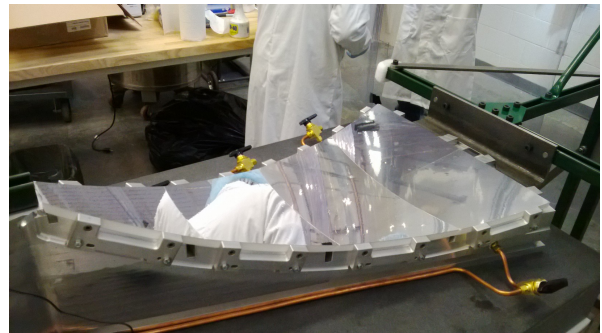


Fig. 23: Fully assembled half-sector mirror. The largest mirror consists of two mirror facets that have the same geometry.

design.

For final mirror assembly we had to build 12 identical half-sector assembly tables and put them together due to the relatively large overall dimensions of the HTCC mirror. The only difference between the high-accuracy half-sector assembly table and the 12 identical tables for the final assembly was that they did not have the side plates. Figure 26 shows one of the 12 vacuum tables made of medium density polyurethane foam with 100% closed cells.

The top portion of the table is made of one solid block of polyurethane foam. It is glued to a 1-in thick wedge-shaped flat aluminum plate. To avoid or minimize possible warping we used plates of 1100 aluminum alloy. The smoothness and accuracy of manufacturing the top surface of the table ensured the ability of the table to firmly hold the half-sector mirror. No gaskets of any kind were used to enhance the holding ability of the table. On the working surface of the vacuum table there are five



Fig. 24: Light collection pattern on the focal plane. The laser beam is rasterized in the plane crossing the mirror covering polar and azimuthal angles in the range of  $\theta = 5^\circ - 12.5^\circ$  and  $\phi = 0^\circ - 30^\circ$ , respectively.



Fig. 25: Light collection pattern on the focal plane for the mirror covering polar and azimuthal angles in the range of  $\theta = 27.5^\circ - 35^\circ$  and  $\phi = 0^\circ - 30^\circ$ , respectively.

independent circular grooves through which air is pumped out under each of the five mirror facets of the half-sector mirror.

The entire set of 12 half-sector vacuum holding tables was assembled on two identical 1-in thick flat plates carrying 6 tables each. These plates were mounted and aligned on the top of a 10 ft by 10 ft granite table. Figure 27 shows the vacuum table for the assembly of the combined HTCC mirror fully equipped with the 60 pumping control valves (5 valves per half-sector). We had to provide tight ambient control (dust level, temperature, and humidity). The table was also equipped with a transparent hood (not shown in Fig. 27) to cover the entire table to run tests at different relative humidities.

It was decided not to equip the table with any devices to check the geometry of the HTCC mirror during assembly. Since the 12 assembled half-sectors passed tight quality controls, there was not much room available for adjustment of the half-sectors on the final assembly table within more than about 0.030 in in the radial direction and within gaps between adjacent half-sectors of about 0.010 in. The geometry was essentially established and fixed once all 12 half-sectors were held tight on the table.

The assembly procedure was the same used before for the half-sectors. The only difference was that we had to install in the center of the combined mirror the lightweight central ring (0.055-in thick) made of carbon fiber. The ring was glued to all



Fig. 26: One of the 12 polyurethane half-sector holding tables.

half-sectors. We controlled and measured the gaps between all adjacent mirror facets belonging to adjacent half-sectors. The average gap was 0.0096 in and is very close to the design value of 0.008 in, which represents the “dead” zone between the half-sectors. The HTCC covers almost 100% of the azimuthal angular acceptance of the CLAS12 Forward Detector. It has to be mentioned that the average gaps between adjacent facets in a given half-sector mirror were 50% smaller, which provides for nearly complete coverage in the polar angle.

The final assembly of the combined HTCC mirror started with applying the epoxy glue on the first half-sector as shown in Fig. 28, using the same procedure employed for the assembly of the half-sectors. Figure 29 shows the partially assembled combined mirror.

We used a special procedure to glue the last half-sector because otherwise we would have had to in-



Fig. 27: All 12 half-sector vacuum tables assembled on their 1-in aluminum plates placed on the granite table.

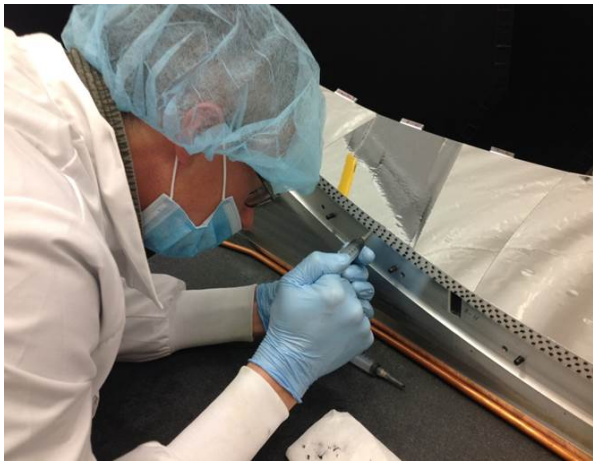


Fig. 28: The dots of epoxy glue being applied to only one side of the half-sector mirror assembly.



Fig. 29: Partially assembled combined HTCC mirror.



Fig. 30: Separated halves of the combined mirror before final gluing.

sert the last half-sector in a very narrow space that would have smeared the glue dots. Therefore, we assembled the first 6 half-sectors on the first 1-in mounting plate, and the remaining 6 half-sectors on the other 1-in mounting plate. The mounting plates with the 6 half-sectors were positioned on the granite table leaving a gap about 1-in wide (see Fig. 30). Epoxy glue was then applied to the one of the exposed sides, (see Fig. 31), and the plates were slid together so that both sides come in contact. Figure 32 shows the completed mirror.

All elements that support and hold the combined mirror are out of the acceptance of the HTCC (see Fig. 33). The rigid, lightweight, composite supporting ring (strong-back) was attached to the combined mirror via 12 composite lightweight bridge pieces glued to the sides around of the mirror. A rendering of the completely assembled HTCC mirror, ready for installation, is shown in Fig. 34. Since the rigidity of the supporting parts is much higher

than the rigidity of the combined mirror, we used flexible silicon compound for gluing.

### 3.6. HTCC Gas Volume Entry and Exit Windows

There are several aspects that have been taken into consideration that define the design of the entry and exit windows:

- Large area to cover;
- Small thickness;
- Opaque;
- High durability;
- Attachment to the main frame;
- Structural stability, i.e. resistance to pressure variations.

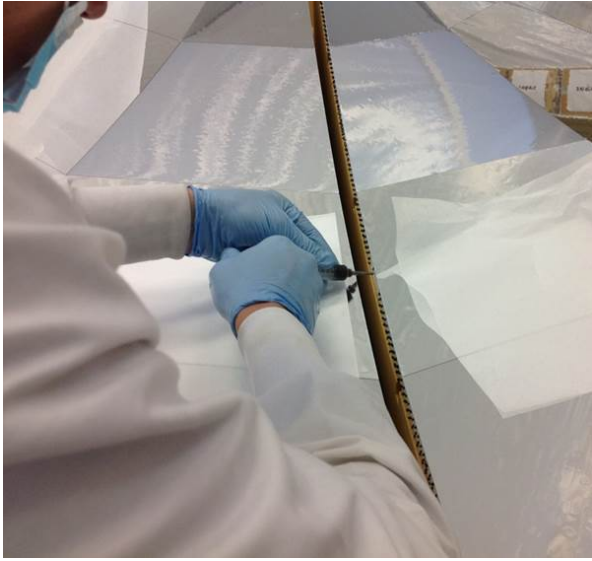


Fig. 31: Application of the epoxy glue on the side of the separated halves of the combined mirror.



Fig. 32: Fully assembled combined HTCC mirror.

The entry and exit windows are composite films made of three layers laminated together: Tedlar (thickness  $38 \mu\text{m}$ ), Mylar (thickness  $75 \mu\text{m}$ ), Tedlar ( $38 \mu\text{m}$ ). The composite films came in rolls 61-in wide. To make the exit window, three composite films were glued together side by side. The glue joint between adjacent composite films was made in such a way that the thickness of the joint exceeded the remaining portions by no more than 10%. The usage of two black Tedlar films in the composite window guaranteed light insulation even if one layer had any holes. One layer of Mylar film provided excellent durability and flexibility.

The dimensions of the entry and exit windows are  $\approx 2.5 \text{ ft}$  and  $\approx 9.5 \text{ ft}$ , respectively, so the difference is significant. This required developing a special design for their attachment to the body of the detector. The primary electron beam passes through the HTCC exactly along the axis of the detector. To decrease the background of Møller electrons we have used a long shielding piece made of tungsten around the beam that nominally covers polar angles up to  $2^\circ$  and has a small cylindrical opening in the center that goes all the way through and is big enough for the beam [4]. The volume of the HTCC must be separated from the volume occupied by the tungsten metal shield. Since the corresponding HTCC part called the Møller Cup that is concentric with the tungsten absorber must be lightweight, the joints between this part and the entry and exit win-

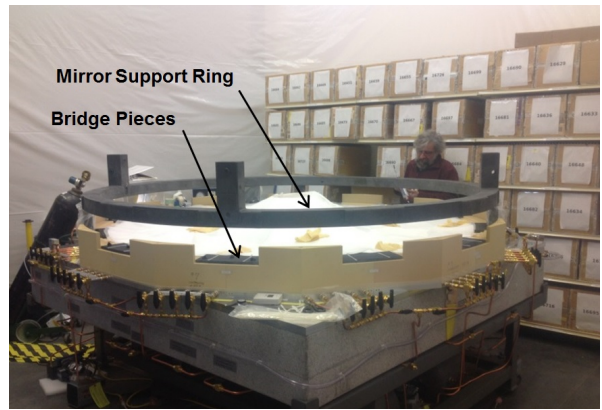


Fig. 33: Supporting elements ready to be attached to the combined mirror. The mirror is covered with soft paper towels to protect the working surface from debris.

dows must also be lightweight. In this case, since the windows have different dimensions, any changes in atmospheric pressure would cause both windows and the Møller Cup attached to them to move upstream or downstream - depending on atmospheric pressure changes. The mirror could be damaged by the exit window if the pressure goes up, or it could be damaged by the conical Møller Cup if the pressure goes down (see Fig. 35). Thus the Møller Cup has to be kept in the same location relative to the mirror regardless of the fluctuations in atmospheric pressure. Even small changes of  $\sim 1 \text{ mm}$  of Hg would generate a force of  $\sim 200 \text{ lbs}$  acting on the Møller Cup along its axis.

To avoid potential problems with the integrity of the detector, the Møller Cup was attached to the main frame of the HTCC at 12 points: 6 points on

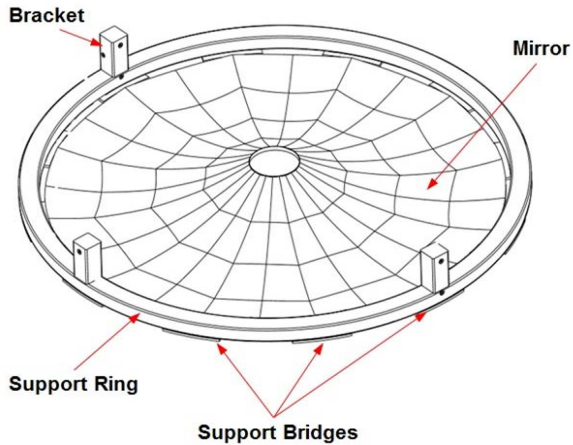


Fig. 34: Completely assembled HTCC mirror ready for installation.

the upstream portion of the main frame, and the remaining 6 points on the downstream portion. All parts providing attachments of the Møller Cup to the front or to the back of the main frame are completely located in the shadow zone of the 6 superconducting coils of the torus magnet [5], i.e. they do not create any obstruction to the particles going through the drift chambers. The Møller Cup was attached using 12 thin spokes, each 1.5 mm in diameter and was made of carbon fibers to minimize the possible scattering of particles traveling within the shadow of the torus coils. The spokes very firmly hold the Møller Cup in position. Each of them was tensioned as necessary to provide structural rigidity and to withstand the stresses generated by the attached windows during atmospheric pressure changes. They were tensioned as a string in order to eliminate any possible damage due to deformations of the body of the HTCC while transporting, installing, or aligning. Each spoke is spring-loaded from both ends. Figures 36 and 37 show the upstream and downstream views of the HTCC with the entry and exit windows installed.

### 3.7. Containment Vessel and Combined Mirror Installation

The HTCC Containment Vessel has properties to satisfy a number of requirements, which included the safe transportation of the fully assembled HTCC to the experimental hall without any changes in the alignment of the internal components and the preservation of the mirror integrity. We tested the integrity of the spare mirror (see Fig. 38)

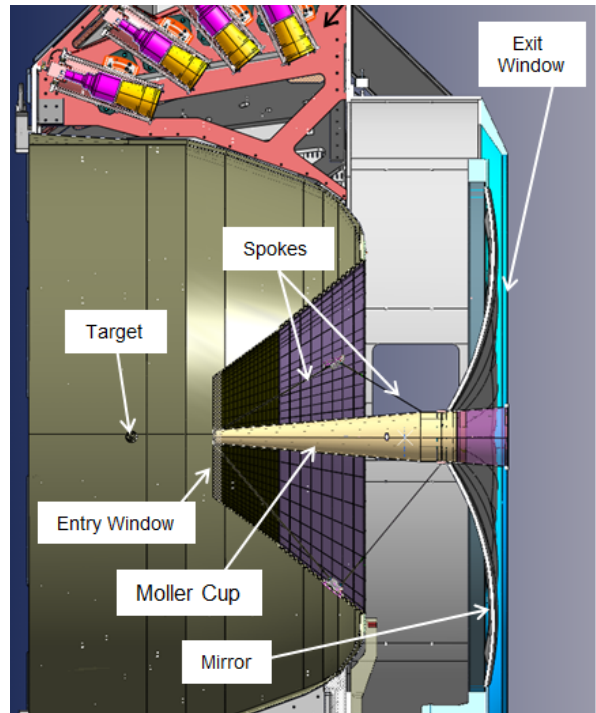


Fig. 35: Side view of the HTCC. The entry and exit windows are shown along with other internal components. The beam is incident from the left.

by transporting it along the chosen route. We successfully transported the detector using the results obtained during the test.

The vessel had to be rigid, have negligible deformation while changing its orientation and, at the same time, allow easy access to any internal components. There is one special requirement for the mirror support structure. The Containment Vessel has only a limited rigidity and even small deformations could directly lead to a dangerous deformation of the HTCC mirror if it was attached to the Containment Vessel directly in ordinary ways. Even if the mirror remains whole and without any cracks, the light collection pattern could still be changed and decrease the signal strength.

In general the vessel works as the support structure for all internal components and must be both light-tight and gas-tight. Safety considerations require that we have both easy and safe access to the components inside. This is absolutely necessary during maintenance and while running alignment checks. Special attention was paid to the routing of cable and fiber optics inside the volume. These items are very difficult to replace. The vessel is

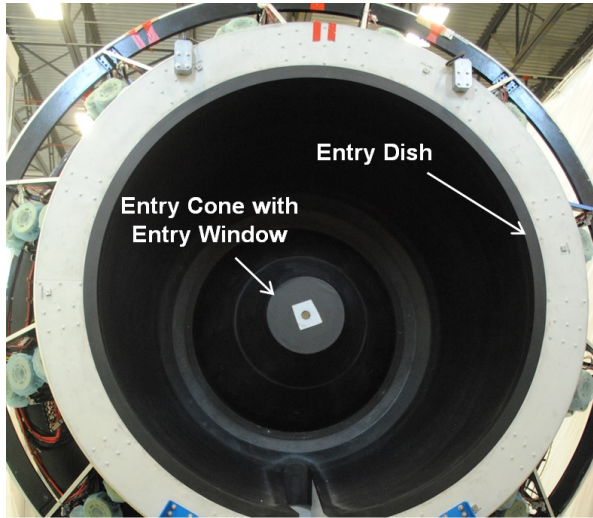


Fig. 36: Upstream view of the HTCC.

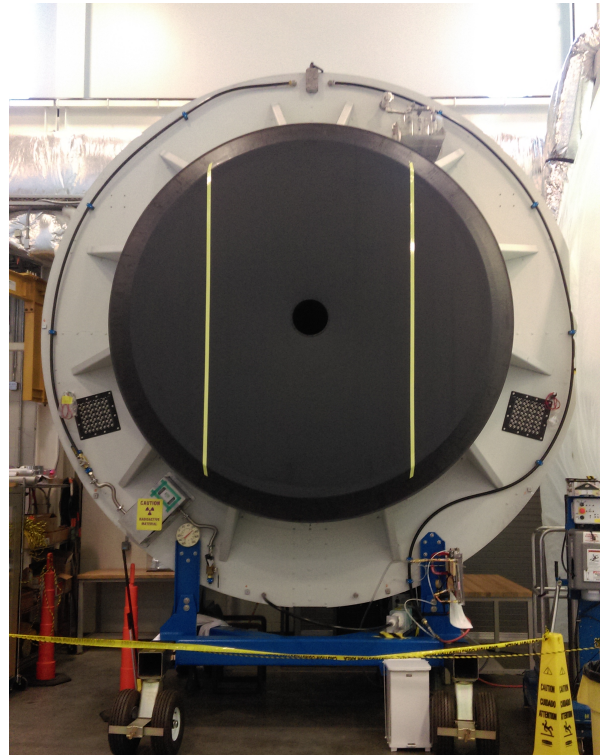


Fig. 37: Downstream view of the HTCC.

755 equipped with a local gas distribution and a control panel. The control panel is for safe and continuous purging of the volume with different dry gases (as needed) and used to keep the water vapor concentration level under tight control during both operations and maintenance.

760 There was a need to have easy access to any of the 48 photomultiplier tubes (PMTs) to adjust their alignment and for maintenance. The Containment Vessel has 24 service hatches wide enough to perform work on any channel. Each channel consists of a PMT with high voltage divider, magnetic shield with compensation coil, and Winston cone, which are installed in the PMT mounting fixture together as one unit, (see Fig. 39).

770 Checks of the cabling and installed fiber optics used for calibration of the PMTs can also be done using the service hatches. Service work can be performed on the detector while it is in its nominal working location. Any access to the internal components of the detector requires replacement of the working gas with dry air. For safety a procedure of purging the HTCC volume has been established to allow access only when the concentration of oxygen in the volume exceeds 19.5%.

780 The combined HTCC mirror is supported and held in the Containment Vessel by 6 orthogonal links. These links connect the supporting ring (attached to the mirror) to the Containment Vessel. It was critical that any deformation of the Containment Vessel not be transmitted to the mirror. Each link has a ball-end swivel on each end. By using

790 the minimum number of links (6) to constrain all motion, the mirror could be aligned, but no forces above those due to gravity on the mass of the mirror and its strong-back are ever placed on the mirror. The set of links are attached to the Containment Vessel at 3 points that are spaced  $120^\circ$  around the perimeter of the ring. This scheme of attachment was tested using a very lightweight 5-ft diameter flat mirror. The tests showed that the light collection pattern stays unchanged within a sufficiently wide range of deformations of the frame that supports the mirror. Therefore possible deformation of the Containment Vessel during installation and alignment do not affect the original shape of the HTCC mirror. Figure 40 shows the HTCC mirror installed in the Containment Vessel.

805 The HTCC is susceptible to noticeable deformations due to the large overall dimensions of the detector. The light and gas leak protection measures provided thus had to be reliable and require little maintenance. All of the inside surfaces of the Containment Vessel have been painted a flat black to reduce light reflectance, and all of the borders between adjacent parts that form the outside shell of the detector have been sealed with a flexible black



Fig. 38: Road tests of the spare mirror.

silicone gel on both the inside and outside of the vessel. Sealing all of the inside seams was necessary to allow the detector to always stay under a positive differential pressure during variations in the atmospheric pressure. As a result of even small changes in the differential pressure, the vessel would be deformed due to its large volume, i.e. the pressure is applied to a large surface area.

### 3.8. Alignment of the Light Collection Components

The HTCC contains light collection and light detection components: the mirror, Winston cone light concentrators, and photomultiplier tubes (PMTs). Even if the mirror is constructed and installed properly as designed, final checks of the component alignment are needed. We have conducted comprehensive checks of the light collection optics on the fully assembled detector. This work was done before the detector was moved to the experimental hall. For the alignment checks we again used a low-power laser, gimbal mounted in the target position. To operate the laser we used a set of standard high-precision devices to control the position and orientation of the laser. The opaque entry window was replaced with a thin transparent film in order

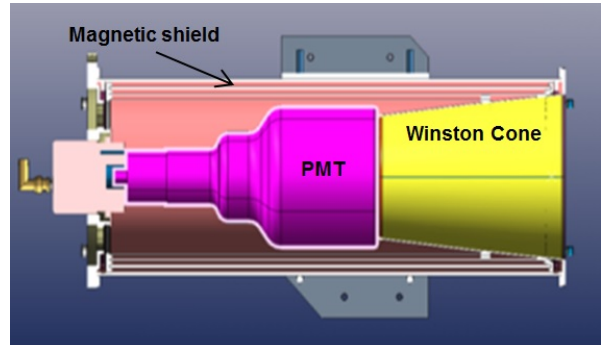


Fig. 39: PMT mounting unit with components.

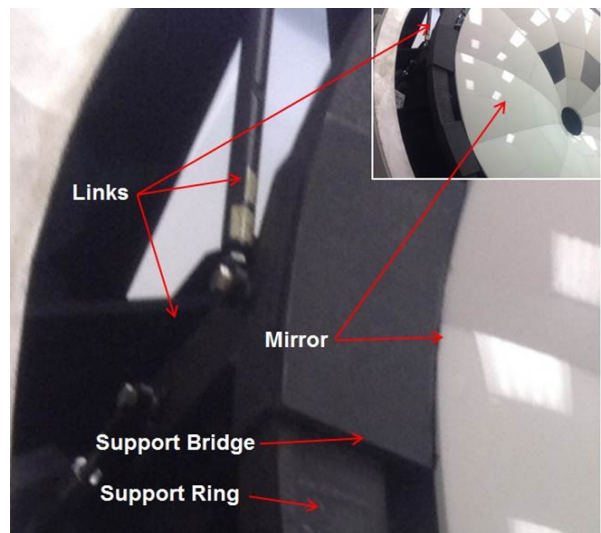


Fig. 40: Combined mirror installed in the Containment Vessel. The set of links holding the mirror in position allow for fine adjustment with an accuracy of  $\sim 0.01$  in or better.

to keep the volume of the detector isolated as much as possible. We opened one access hatch at the time for short periods of time to install templates on the face of the accessible Winston cones and perform adjustments of the housing units each containing a 5-in PMT, Winston cone, 3-layer magnetic shield, and compensation coil. The alignment of all 48 PMT housing units was checked and adjusted as needed.

Each mirror facet was illuminated with the laser at 5 points: the center of the facet and its four corners, and the reflected light pattern was photographed. For some of the channels we checked the light collection geometry at normal relative humidity in the HTCC volume and at 0% relative humidity.

Figure 41 shows the pattern of the light reflec-

tion when mirror facet #3 was illuminated in the center. Circles of diameter 1 in, 3 in, and 5 in concentric to the PMT are shown. The result was obtained at normal relative humidity. Results obtained at RH=0% for the same channel show small but acceptable differences (see Fig. 42). Similar geometry test results were obtained for channel #4 covering polar angles in range of 5° to 12.5°. They are shown in Figs. 43 and 44 obtained at different relative humidities.

Considering the light collection patterns obtained when the mirror facets were illuminated in the corners we made the necessary adjustments in the alignment of the PMT mounting units. No adjustments were needed for the HTCC mirror. Figure 45 shows the test results for mirror facet #3 from sector 5, half-sector 1 obtained before adjustments in alignment were done. Figure 46 shows the changes in the light collection pattern after the alignment adjustments. The image has been shifted toward the center. Figure 47 shows a photograph taken when the mirror was illuminated in the center. The five circles concentric to the PMT shown in the photograph have diameters from 1 to 6 in.

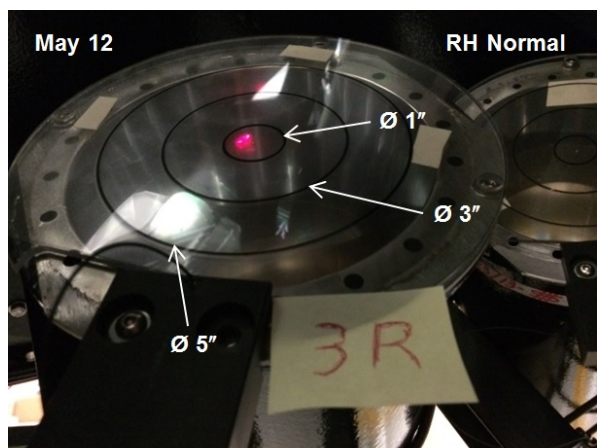


Fig. 41: Geometry test result for channel #3 covering polar angles from 12.5° to 20° at nominal relative humidity. The corresponding mirror facet was illuminated in the center.

Figure 48 shows the final light collection patterns obtained for all mirrors for half-sectors 1 and 2 from sector 5. One can clearly see that the light collection is more focused for the small mirrors than for the large ones. This effect is caused by the difference in the rigidity between the combined mirror itself and the supporting ring attached to it, as well as the different sensitivities to the changes in rela-

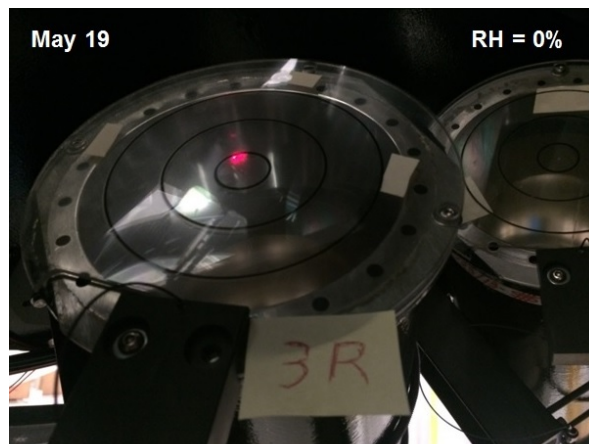


Fig. 42: Geometry test result for channel #3 covering polar angles from 12.5° to 20° at RH=0%. The corresponding mirror facet was illuminated in the center.

tive humidity of the environment.

Since the mirror has a funnel shape, see Fig. 49, the nose of the funnel gets stretched less than outer portion of the mirror. The outer portion of the mirror consists of mirror facets #1 and #2, the largest mirror facets. Even though the widths of facets #1 and #2 measured in the radial direction are close to each other, the effect of humidity changes for the outermost facet #1 is larger than for facet #2 due to the funnel shape of the combined mirror.

### 3.9. Gas Composition Control

The fully assembled detector was tested for gas and light leaks. Gas tightness was checked by filling the volume with a mixture of dry air and a small amount of non-flammable gas at positive differential pressure. Freon gas leak sniffers were used. As expected, most of the leaks were found around the entry and exit windows because both windows were sealed only from the outside as they were the last two components attached to the Containment Vessel. Light tightness was checked by monitoring the counting rates of the photomultiplier tubes while illuminating the sealed seams of the vessel with an external light source. The rates were close to the dark counting rates whether the lights in the hall were turned on or off. The gas tightness was controlled by fixing the leaks found and then by measuring the humidity inside the detector while it was continuously purged with dry nitrogen. At flow rates of 10 - 15 l/min, a humidity level not higher than ~100 ppm was measured in a span of 2-3 days

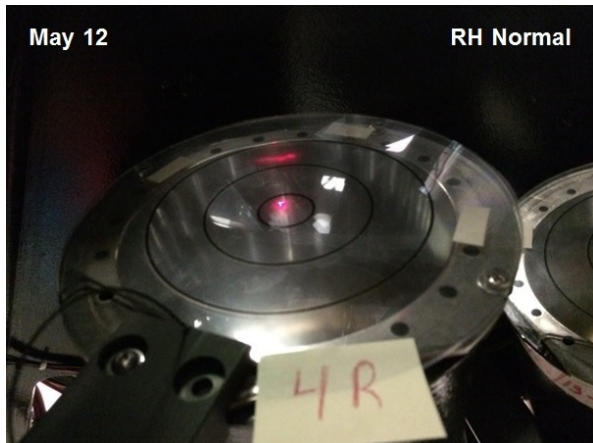


Fig. 43: Geometry test result for channel #4 covering polar angles from  $5^\circ$  to  $12.5^\circ$  at nominal relative humidity. The corresponding mirror facet was illuminated in the center.

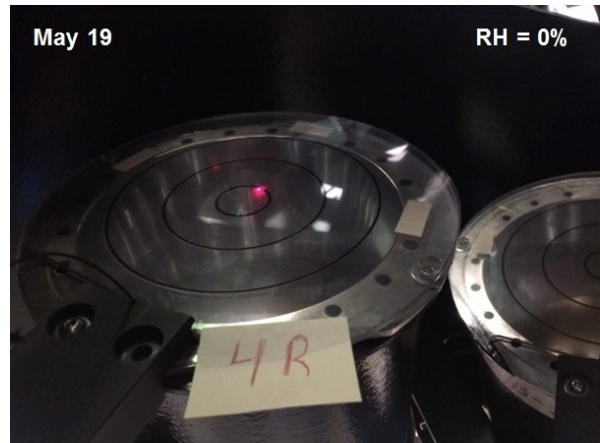


Fig. 44: Geometry test result for channel #4 covering polar angles from  $5^\circ$  to  $12.5^\circ$  at  $RH=0\%$ . The corresponding mirror facet was illuminated in the center.

of continuous purging. These results can be used as a good indication of a low level of water vapor and oxygen content. Note that the diffusion of water vapor and oxygen through the windows is defined by the Tedlar films, which have the lowest diffusion coefficients. For Tedlar the diffusion of oxygen is lower than the diffusion of water vapor. The presence of water vapor and oxygen in the working volume is unavoidable but should be kept at the lowest possible level because water vapor and  $CO_2$  gas produce carbonic acid that may be harmful to the mirror working surface. As far as oxygen content is concerned, it also needs to be kept at the lowest possible level. During operations with beam a certain amount of ozone can be generated due to radiation. Both oxygen and ozone absorb the ultraviolet component of Cherenkov light in the HTCC generated by scattered electrons. Consequently the signal strength becomes lower, which directly leads to a reduced electron detection efficiency and a reduced rejection of charged pions.

Another reason to keep tight control on humidity is related to the sensitivity (to some extent) of the mirror shape to humidity. The mirror must be used at the lowest humidity level, but the entire manufacturing process of the mirror facets was done at normal room conditions. Once the mirror had been installed, the HTCC volume was sealed and purged with dry gas ( $N_2$ ,  $CO_2$ , or dry air). Altering the humidity from almost zero to normal atmosphere conditions may lead to component fatigue and cause structural deformation. During mainte-

nance the volume is partially exposed to the outside environment, which increases humidity. In any case, all maintenance activities are stopped once the relative humidity inside the volume reaches 2-3%. This is controlled at the exhaust of the detector. Maintenance is resumed only after the operational humidity level is restored.

The detector is equipped with a local gas control panel. The parameters that can be read directly are limited to the pressure at the input of the volume and the differential pressure. The HTCC is continuously monitored online by a system that monitors the following parameters:

- Type of gas;
- Gas flow rate;
- Differential pressure;
- Humidity;
- Amount of gas already consumed.

The online control system allows the detector to be safely operated within predefined intervals of parameter variations. This system generates warnings and alarms that require either remote or in situ response. In the case of a power outage in the hall, the mass flow controller turns off and purging is stopped. It takes several hours for the humidity to rise up to 2-3% due to direct leaks and diffusion of the ambient humid air inside the working volume. This provides enough time for operation to switch

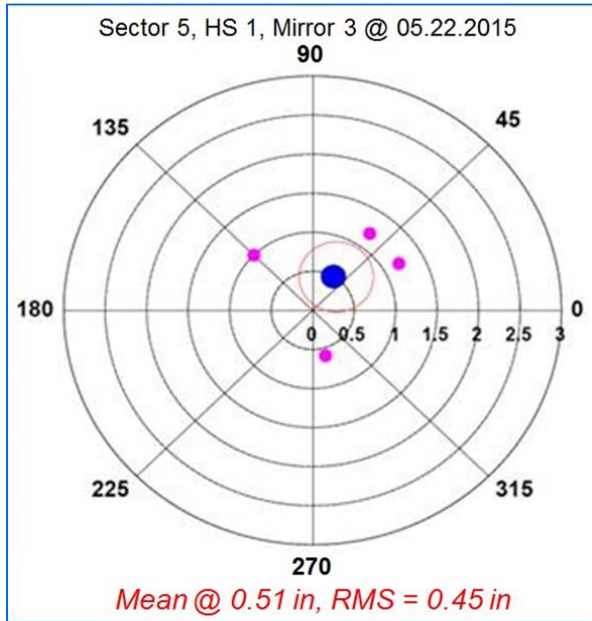


Fig. 45: Geometry test result for sector 5, half-sector 1, mirror #3 covering polar angles in range of  $12.5^\circ$  to  $20^\circ$  obtained before adjustment when mirror #3 was illuminated in the center (blue), and its corners (purple). The black circles are 1 in to 6 in in diameter. The circle (red) is of radius 0.45 in, and is equal to the RMS of the fitted center of gravity of the light collection pattern.

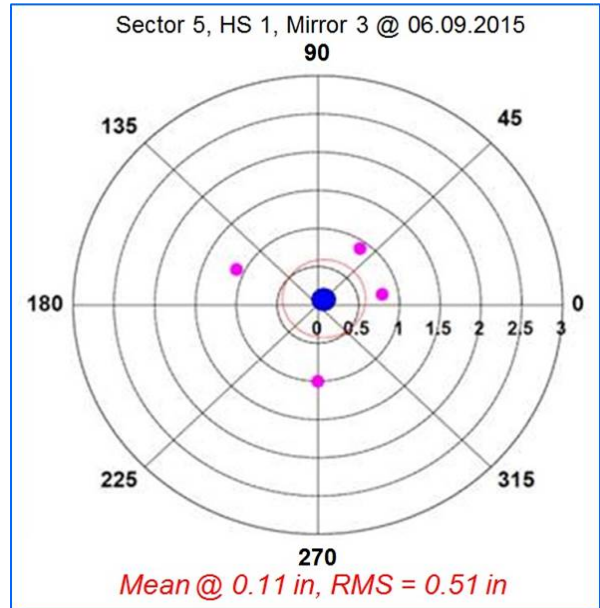


Fig. 46: Geometry test result for sector 5, half-sector 1, mirror #3 covering polar angles in range of  $12.5^\circ$  to  $20^\circ$  obtained after adjustment when mirror #3 was illuminated in the center (blue) and its corners (purple). The black circles are 1 in to 6 in in diameter. The circle (red) is of radius 0.51 in, and is equal to the RMS of fitted center of gravity of the light collection pattern.

the gas to a manual bypass rota-meter, which is normally closed. The local gas panel includes three specialized filters that prevent dust, water vapor, and oil vapor from entering the volume.

## 4. Electronics and Light Monitoring System

### 4.1. Electronics

The electronics of the HTCC provides spectrometric and timing information for electron scattering events that are detected by the HTCC within its acceptance. Two fast output signals are required from each channel in order to generate a fast trigger for the CLAS12 spectrometer [6]. This required that the anode signal from the PMT had to be split or that the voltage divider for the PMT be modified by adding a fast preamplifier to generate two identical signals with the same polarity. In our case we have chosen to use a modified standard linear passive high voltage divider that is equipped with a fast preamplifier (see Fig. 50). This preamplifier is integrated in the original divider and does not need external power supplies other than the same high voltage power supply used for the PMTs. The amplifi-

cation coefficient varies from 8 to 10. The preamplifier provides two output signals of negative polarity. However, the commissioning of the HTCC has shown that the timing resolution achieved from the digitized FADC waveform using a standard pulse-shape fitting algorithm is sufficient to avoid the use of discriminators/TDCs. Therefore the second preamplifier output is not used the HTCC is not used.

The preamplifier is also fast: the signal rise time increases by 1.5 ns as compared with the signal from a passive divider, and it is almost as fast as a signal from fast plastic scintillators. Figures 51 and 52 show typical signals provided by a standard passive divider and by the modified divider, respectively. The pulses have near perfect output termination with no signs of any ringing or after-pulsing.

The preamplifier is compact and reliable, and does not require any changes in the high voltage power supply or in the cabling/connection scheme. It consumes relatively low current and does not need additional cooling.

It has to be mentioned that the preamplifier we use generates additional noise as any other pream-

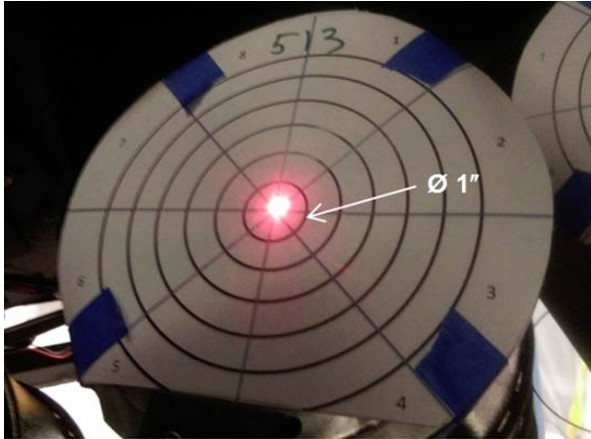


Fig. 47: Geometry test result for the sector 5, half-sector 1, mirror #3 covering polar angles in range of  $12.5^\circ$  to  $20^\circ$  obtained after adjustment when mirror #3 was illuminated in the center.

plifier unavoidably would. However, this additional noise is not an issue due to the much larger noise contribution from the 5-in PMTs used for the HTCC. These PMTs were so noisy that it was impossible to observe any indication of a single photoelectron peak. Figure 53 shows the calibration results for a representative PMT with a modified divider.

#### 4.2. Light Monitoring System and Signal Readout

In order to gain match phototubes that do not directly reveal the single photoelectron signal, we developed a new external very fast light source with Light Emitting Diodes (LEDs). Figure 54 shows all components of the HTCC Light Monitoring System (LMS). The device is remotely driven, allows for changes in the emitted light intensity, and works at different frequencies in a wide range of these parameters. Once turned on, and after temperature equilibrium is reached, the source is very stable in providing light signals with the required strength and timing. There is an LED panel installed at the entry window of a 4-in diameter integrating sphere. This panel illuminates the sphere and the light is distributed evenly between 50 coated clear optical fibers that are 1 mm in diameter that form a bundle. All the fibers in the bundle have the same length and direct the light onto the face of the PMT. The average light intensity is monitored and kept very stable during the entire period of measurements. The average amplitude was at the level of a few photoelectrons. Since it is possible to adjust the

frequency of the light pulses, we were able to observe PMT signals that were well separated from the dark noise.

The valuable features of the LMS and of the procedure for gain matching the phototubes are:

- The system can be used to calibrate either low-noise or high-noise PMTs;
- The LMS generated calibration light intensity was kept stable during data taking;
- It is only necessary to have the fiber optics deliver light intensity to all channels with 10-20% uniformity;
- The calibration results are reproducible even if one uses different settings for the LED source;
- Maintenance of the LMS is essentially simplified since calibration of the LMS itself is not needed;
- Possible usage of the LMS as often as needed without the necessity of providing the same intensity of light source in different calibration sessions.

The typical frequency of the LED light pulses is in the range of 6 to 10 kHz and is defined by a standard pulse generator. The results obtained during the CLAS12 commissioning run and the following physics run with an electron beam have shown that the information provided by the JLab proprietary FADC250 modules (250 MHz Flash ADCs) [7] for the HTCC signal strength and timing is sufficient.

## 5. Calibration and Event Reconstruction

### 5.1. Gain Calibration of PMTs

We use ET 9823QKB PMTs that have a dark current up to 1000 nA as specified by the manufacturer. At a nominal high voltage of  $\sim 2,400$  V, it was impossible to observe a single photoelectron peak due to the high dark noise rate. Therefore we developed a special procedure for the gain calibration of the PMTs. We have implemented a method of fitting and extracting the position of the single photoelectron peak using the parameterization described in Ref. [8].

Figure 55 shows the main definitions for the analysis of a representative PMT response obtained with the LMS to extract the position of a single

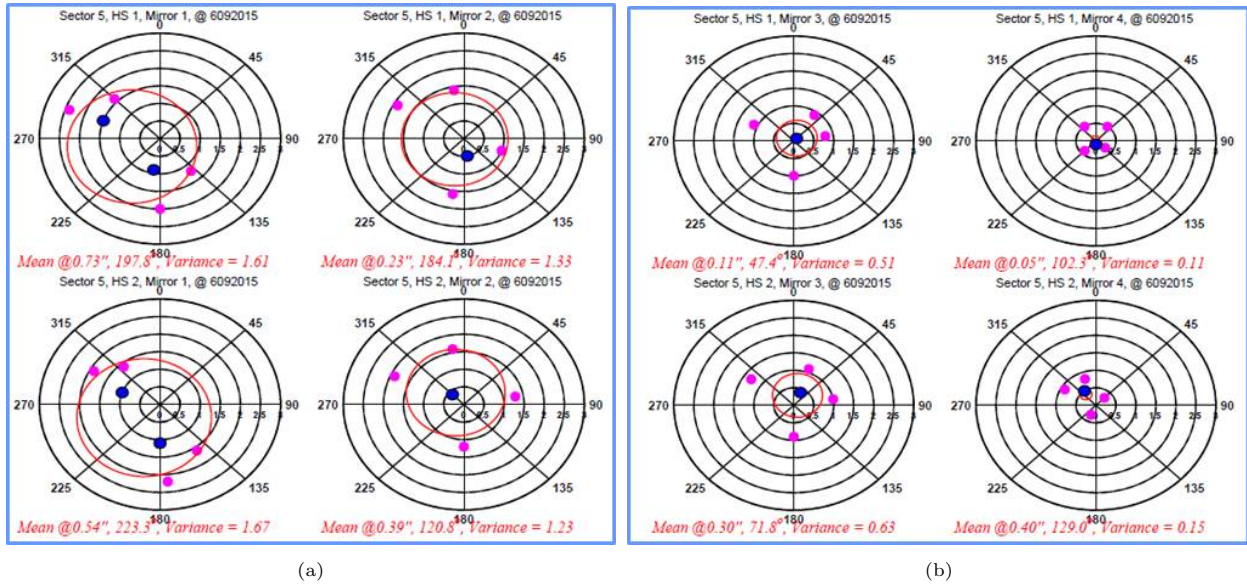


Fig. 48: Light collection test result for both half-sectors of sector 5. (a) - Mirrors #1 and #2 cover polar angles in the range of  $20^\circ$  to  $35^\circ$  within an azimuthal interval of  $60^\circ$ . (b) - Mirrors #3 and #4 cover polar angles in range of  $5^\circ$  to  $20^\circ$  within an azimuthal interval of  $60^\circ$ . The data are shown after adjustment of the light-collection optics. The mirrors were illuminated in the center and the corners.

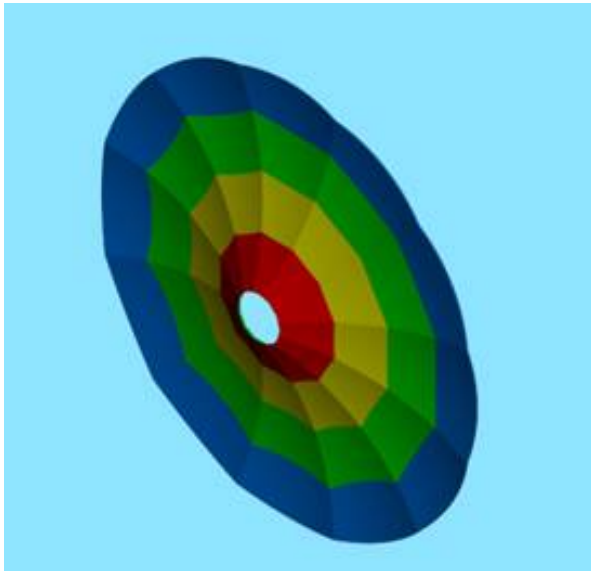


Fig. 49: The combined HTCC mirror is funnel-shaped.

photoelectron peak when the average intensity of the LMS light is about few photoelectrons. Figure 56 shows an example of typical fits of the PMT response to LMS light of constant intensity at different high voltages. The corresponding dependence of the single photoelectron peak position as a function of high voltage is given in Fig. 57. Of course

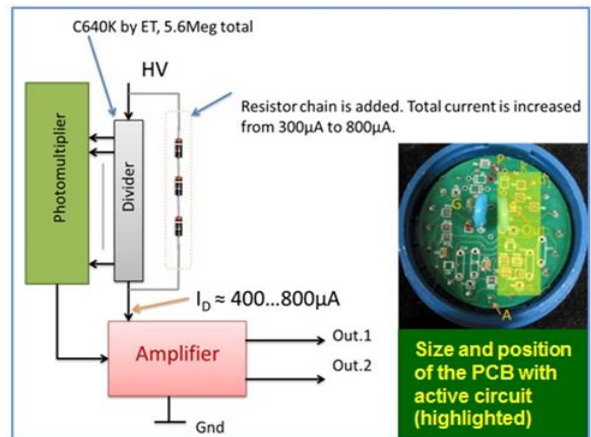


Fig. 50: Modified high voltage divider with 2 identical outputs used for the HTCC.

this method required that the LMS generate light pulses of stable intensity. The results of the single photoelectron peak position can be used for gain matching. Calibration measurements are performed for all PMTs in parallel at the same LMS settings. This can be done by adjusting the high voltage applied to individual channels.

The distinguishing feature of the HTCC LMS is that the observed repeatability of results is within 5-10% of that obtained in runs at different but sta-

1105

1110

1100

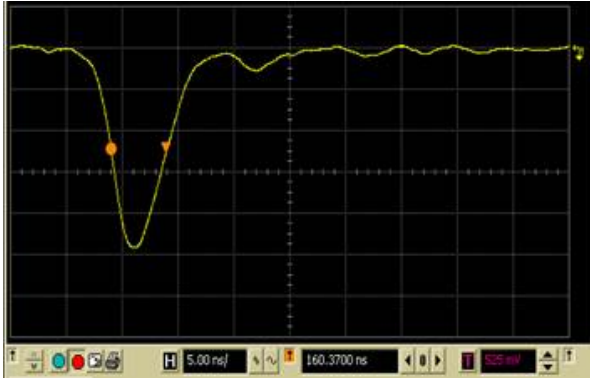


Fig. 51: Typical output signal provided by a passive HV-divider.

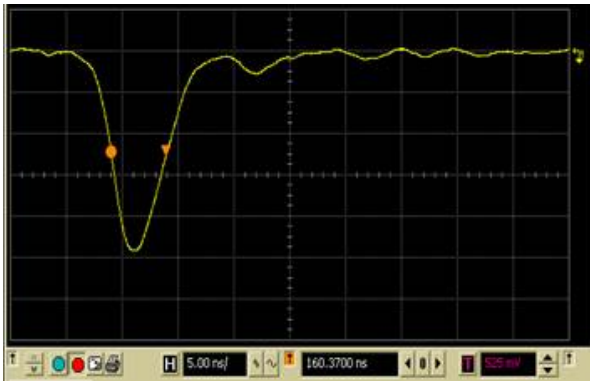


Fig. 52: Typical output signal provided by the modified HTCC HV-divider with 2 identical outputs.

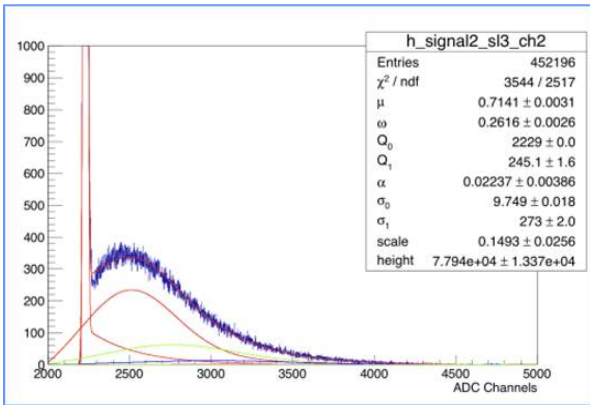


Fig. 53: Calibration results for a representative PMT with a modified divider. The red curves represent a pedestal signal (narrow) and a single photoelectron peak. In most cases the PMTs have been used at lower voltage settings (by about 600 V) than specified for the standard divider.

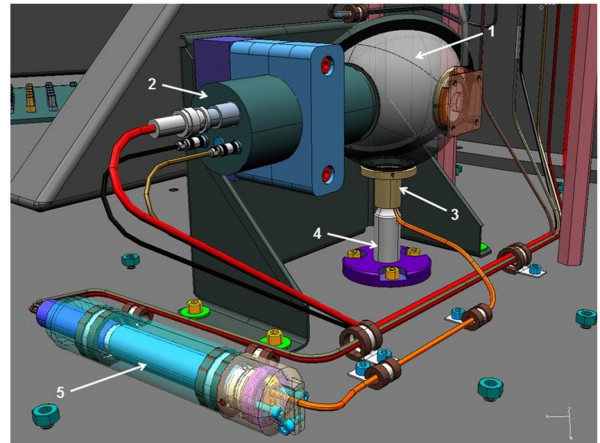


Fig. 54: The Light Monitoring System consists of an integrating sphere (1), fast light source (2), adapter (3), 50 fiber optic cables bundled in a harness (4), and the reference PMT (5).

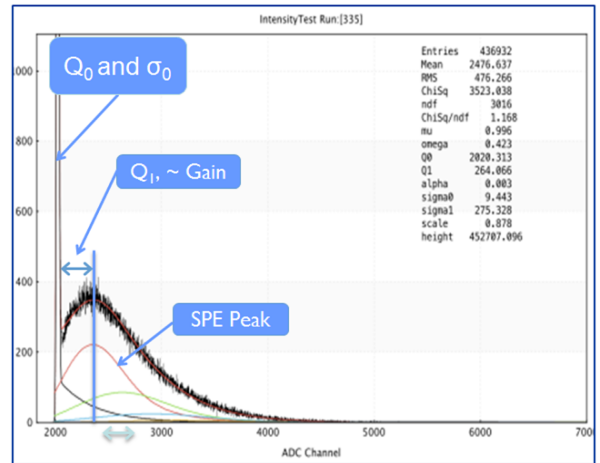


Fig. 55: Definitions:  $Q_0$  and  $\sigma_0$  are the position and width of the pedestal,  $Q_1$  is proportional to the gain of the PMT. The red curve defines the single photoelectron peak. The green and blue curves describe the 2 and 3 photoelectron peaks.

photoelectron peak at different LMS light intensities are shown for a representative PMT at a fixed voltage setting. The fitting function is stable across a wide range of intensities and accurately describes the PMT response at low intensities ( $\mu < 1.0$ ). The position of the peak stays within 5% of the mean. Consequently there is no need to keep the light source intensity uniform, i.e. stay the same or close to the same in different calibration runs that are taken whenever necessary.

We have compared our preliminary single photoelectron calibration results with those obtained

ble light intensities and frequencies. This is demonstrated in Fig. 58 where the positions of the single

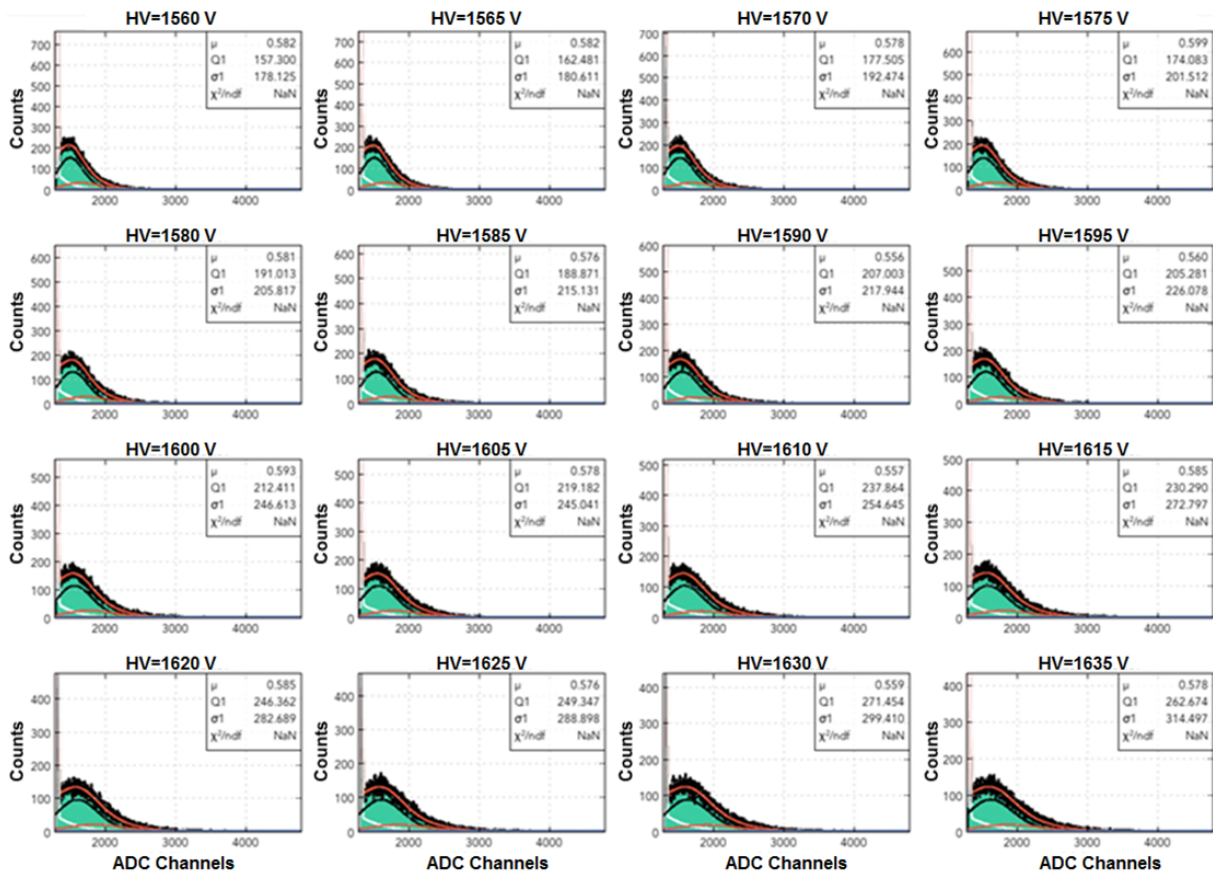


Fig. 56: Response of a representative PMT to LMS light of constant intensity at high voltage settings from 1560 V to 1635 V with a 5 V increment.

using the approach described in Ref. [9]. The same PMT with a modified divider was tested. Each data set was normalized by the average value. Figure 59 shows the results for the 12 PMTs monitoring events in the polar angle range from  $27.5^\circ$  to  $35^\circ$  (labeled as Ring 4) from the 6 sectors. Both approaches provide consistent results, even though the external light sources and software used in the calibration measurements were different.

### 5.2. Response Equalization

Different factors (including imperfections of the mirror working surface, dust deposition, condensation of fumes, overall mirror shape distortions, and gain instability of the individual PMTs) can lead to a variation in the signal strength from the individual channels, even after comprehensive single photoelectron calibration is complete. These variations should be corrected independently of their physical origin, as the trigger efficiency is heavily

dependent on the uniformity of the HTCC response. In the beginning of every physics run period we analyze the first data in order to estimate the signal strength in each of the 48 channels. We then develop corresponding correction factors, which align the signals between individual channels to the average value between channels. These correction factors are then propagated to both the offline reconstruction through the CLAS12 calibration database (ccdb) [10] and the online trigger gain files. Figure 60 shows results for the channel response before and after equalization.

### 5.3. Timing Calibrations

Since the HTCC is the part of the trigger [6], it is required that the timing of the individual channels is aligned to aid the online cluster reconstruction. As a result, the timing calibration of the HTCC is done in two steps: the first step is performed on the

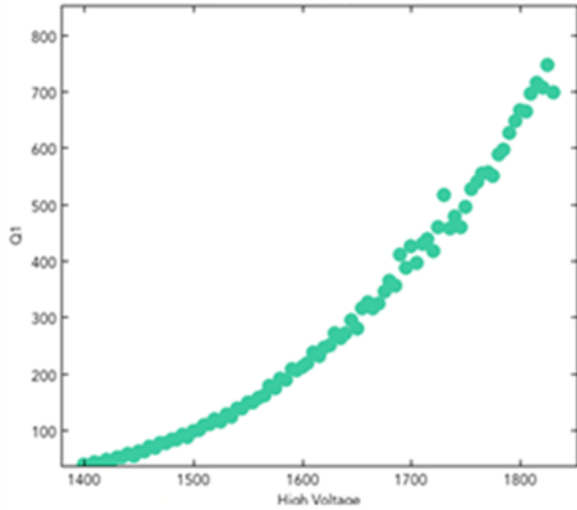


Fig. 57: Single photoelectron peak position as a function of high voltage (V) for a representative HTCC PMT.

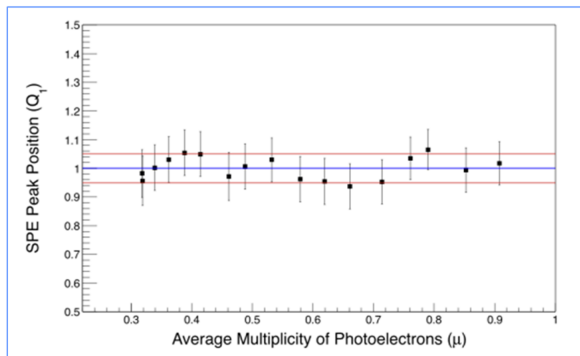


Fig. 58: Single photoelectron peak position as a function of LMS light intensity at constant high voltage for a representative HTCC PMT. The red lines show a  $\pm 5\%$  deviation, and the blue line shows the averaged single photoelectron peak position.

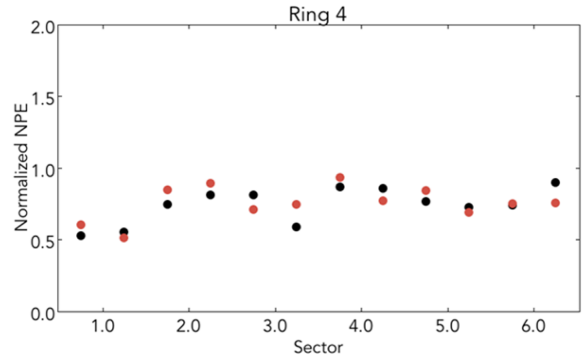


Fig. 59: Comparison of preliminary calibration results using two different fitting codes from Ref. [8] (black dots) and Ref. [9] (red dots).

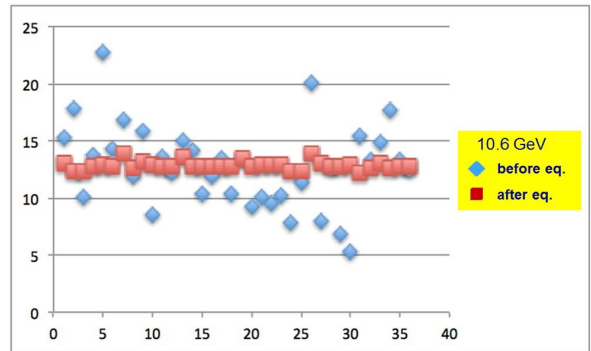


Fig. 60: Response of the PMTs in terms of the number of photoelectrons before and after response equalization.

time shifts are added to the ccdb database and are applied at the reconstruction stage. Figure 61 shows the timing resolution combined over all 48 PMTs is on the level of 0.6 ns.

#### 5.4. Event Reconstruction

The goal of the reconstruction procedure is to reconstruct the real signal strength, time, and hit position from the raw ADC signals. This is done in two steps:

1. In the offline decoding stage: the signal is converted from the hardware notation (crate, slot, channel) into the CLAS12 notation (sector, layer, component) [10]. For each signal, its amplitude (in ADC channels) and timing is determined from the threshold crossing, and the pedestal is subtracted. The pedestal value for each channel is determined during special pedestal runs and is stored for both trigger and offline reconstruction purposes.

1165 level of the FADC, and the second step (finer step) 1185 is done in the offline calibration.

1170 The online calibration is done using the independent trigger from the Forward Tagger detector [11]. The timing of all 48 HTCC channels is aligned in the FADC configuration files by setting the appropriate delays with a precision of 4 ns (the best available using the FADC). Since the timing resolution of individual channels is on the order of about 1 ns, we can achieve better resolution of the detector than the 4 ns available from the FADC. To do so, we calculate the time at the beam-target interaction vertex for each of the 48 channels and estimate the time shift between the individual channels. These 1195

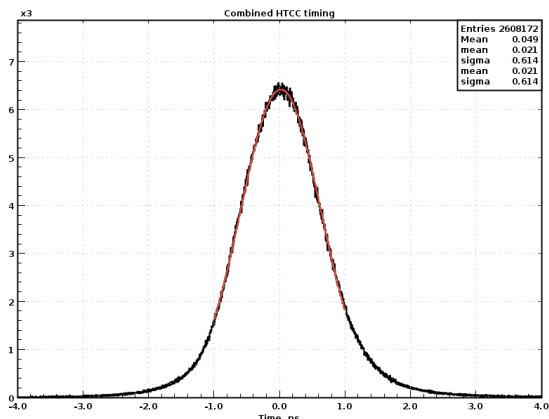


Fig. 61: Combined timing of the 48 HTCC PMTs. The red curve is a Gaussian fit with a width  $\sigma \sim 0.6$  ns, giving the average system timing resolution.

2. In the reconstruction stage: the ADC signal is converted into the number of photoelectrons using the gain constants in the CLAS12 calibration database (ccdb). The physical design of the HTCC allows the Cherenkov radiation from one electron to split into up to four channels (see Fig. 62). In order to reconstruct the signal strength, we need to combine such split signals into a single cluster. We start by selecting the strongest hit for a given event and use it as the starting point of the cluster. We then look for adjacent hits within a certain time window (stored as a parameter in ccdb). If such hits are found, they will be added to the cluster. In the final stage, the signal strength is determined as the sum of the individual signals, and the signal time is determined as the average between the individual signals, weighted by the corresponding number of photoelectrons. The hit angular coordinate is determined as the average between the individual hits forming the cluster. Hits, attributed to the established clusters, are removed from further consideration, and the algorithm continues to look for the next cluster until the list of hits is exhausted. See Ref. [10] for more details.

## 6. Monte Carlo Simulations

Comprehensive Monte Carlo (MC) simulations to check the major parameters of the HTCC were done before the design of the detector was completed.

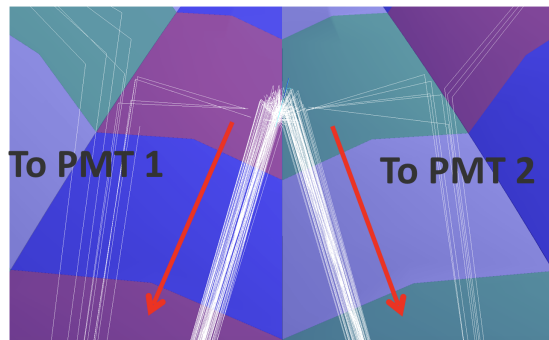


Fig. 62: Splitting of the Cherenkov radiation between two mirrors. Geometrically the signal can split into up to four mirrors.

Electrons of 2 GeV energy were used. The core concept of the goal to reach was to build a detector that had to be installed in front of the forward tracking system as one unit without any support structure in the acceptance. A light collection pattern has been simulated for the exact HTCC geometry of all components, including their properties and detailed specifications of materials to answer the following basic questions with regard to the detector:

- Is the chosen light collection geometry adequate to provide the highest possible electron detection efficiency and efficient rejection of background events?
- Which components (options) would provide acceptable performance of the detector (mirrors, PMTs)?
- What shape (convex or flat) of the PMT window has the most efficient light collection?
- What window material has to be used to provide the highest possible signal strength?
- What are the actual image dimensions in the focal planes?
- What would be the basic dimensions of a Winston cone light concentrator, if we had to use them?

Figure 63 shows the MC simulation results for the properties of the major components of the detector: transparency of the  $\text{CO}_2$  radiator gas, reflectivity of the mirrors deposited with metal aluminum covered by  $\text{MgF}_2$  protection coating, and the transparency of the PMT entry window material as a function of

1260 wavelength. The radiator gas and mirror show good  
 1265 optical properties (transmittance and reflectivity) in  
 1270 the UV range.

As far as the entry window material is concerned,  
 the quartz window provides a larger signal as compared  
 1265 to a window made of UV-transmitting glass. However,  
 PMTs with quartz entry windows are significantly more  
 expensive and are also fragile. We have run comparative  
 1270 tests of 5-in ET 9823 PMTs with both quartz and  
 UV-transmitting glass windows to justify our choice. Figure  
 64 shows the results obtained for the PMT glass transparency.  
 The measurements showed that average signal from a  
 PMT with a quartz window is equivalent to 55.6  
 1275 photoelectrons, whereas for the PMT with UV-  
 transmitting glass, the average signal is only 38.2  
 photoelectrons (i.e.  $\sim 45\%$  more light for the quartz  
 PMTs).

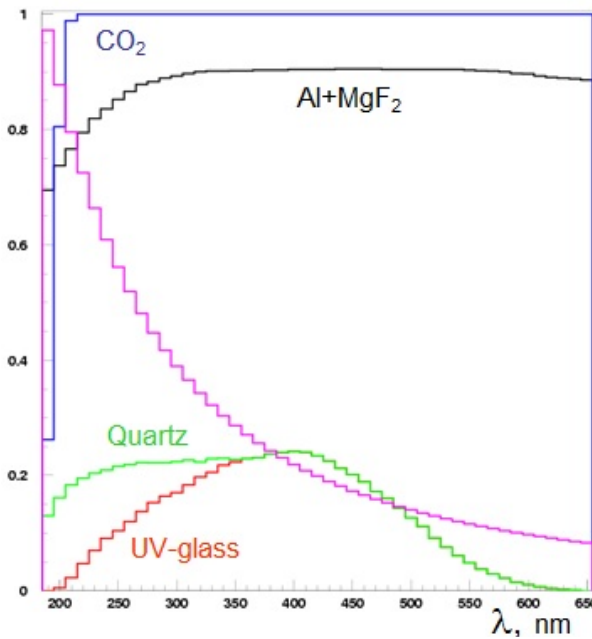


Fig. 63: Optical properties of the HTCC major components in terms of transparency vs. wavelength from MC studies. The exponential histogram (magenta) describes the Cherenkov light spectrum. The blue histogram shows results for the transparency of CO<sub>2</sub> gas and the black histogram shows the reflectivity of the mirror. The results for the response of the PMTs with a quartz face plate (green) and with a UV-transmitting glass window (red) are shown as well.

1280 In the HTCC, Cherenkov light is generated along  
 the entire length of a scattered electron's trajectory  
 in the volume of the detector. The light collection  
 geometry provided by the fully ellipsoidal mirror  
 with point-to-point focusing is valid only in the case

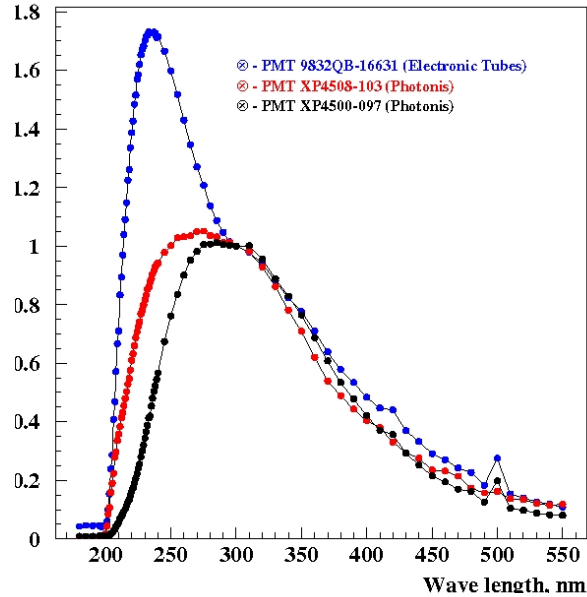


Fig. 64: Comparative measurement test results on the transparency of PMT windows made of quartz (blue), UV-transmitting glass (red), and regular glass (black).

when one focal point is in the target position and when the second focal point is at the face of the PMT. Consequently, one must expect considerable changes in the size of the image in the focal plane due to the continuous evolution of the light emission point along the electron trajectory. Moreover, there is no light emitted by a scattered electron moving from the target until it crosses the entry window of the HTCC. PMTs of large size are available with a face plate (entry window) of various shapes. This is one more parameter to check.

Figure 65 shows simulation results on the collection of light impinging on the entry window for two different PMTs, comparing those with convex windows and those with flat windows. Clearly the flat entry window is preferable. Most of the light has larger angles of incidence for the PMTs with a convex window. Besides, for them a larger portion of the light would undergo two reflections (off the mirror and Winston cone), whereas for the PMTs with a flat face plate, most of the light hits the window under small angles of incidence. From Fig. 65 we also estimated that about 80% of the Cherenkov light will directly impinge on the PMT photocathode and the remaining 20% will first be reflected by the Winston cone. The 5-in quartz ET-9823QKB PMT used in the HTCC has a photocathode that is actually 110 mm in diameter ( $\sim 4.3$  in).

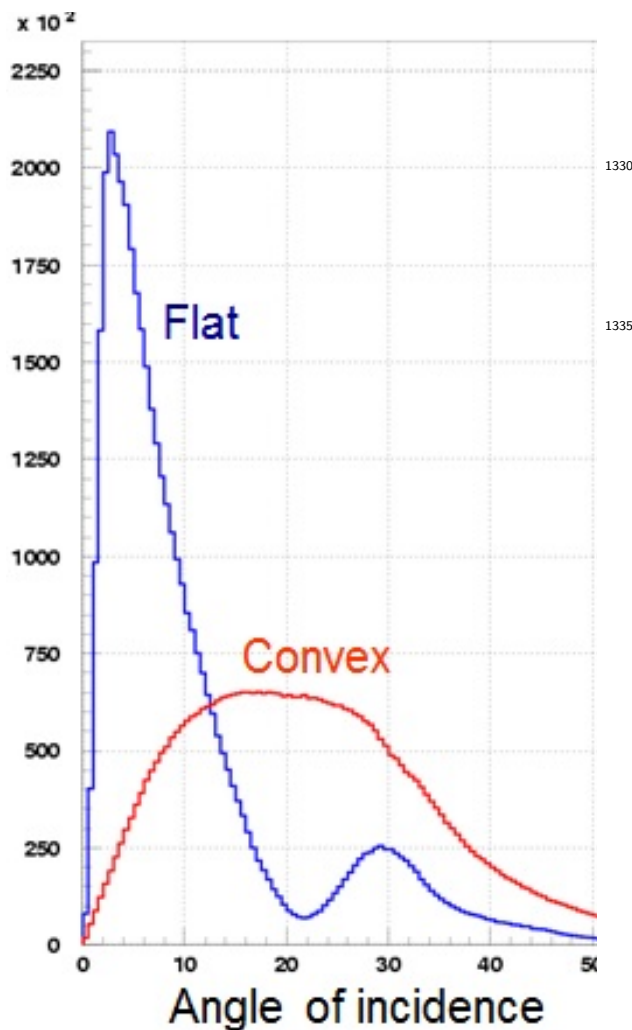


Fig. 65: Distribution of photons impinging on the PMT face plate from MC studies.

Figures. 66, 67, and 68 show the results of the MC simulations for the light collection on the face of the PMT that detects light reflected by a mirror facet that covers a polar angle range of  $5^\circ$  to  $12.5^\circ$ . The simulation results were obtained for 2 GeV electrons on a point-like target with and without the 5 T solenoidal field, and for a 10-cm-long target with the 5 T field. On all three pictures, the circular boundary at 110 mm diameter represents the edge of the PMT light sensitive area. The light collection pattern is not sensitive to the solenoid field, especially if the target is short. The data are presented with a logarithmic scale to show that most of the light impinges directly on the photocathode. In the experiments with the electron beam, the cryogenic

target is typically 5 cm long.

Similar simulation results are obtained for patterns on the face of the Winston cone light concentrators. Figure 69 shows the result for a 10-cm-long target in a 5 T field. There is a circle of diameter 161.4 mm shown on the picture just for illustration of a possible Winston cone opening diameter. Based on these results the Winston cones used in the HTCC have a circular opening of 148 mm diameter and a length of 190 mm.

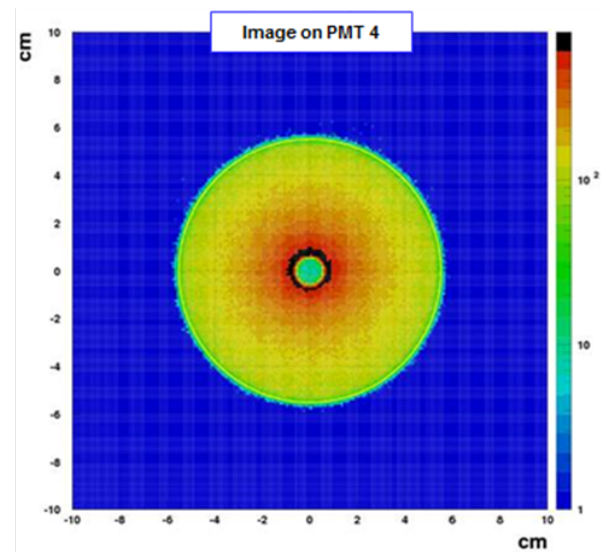


Fig. 66: Simulation result for the light collection pattern on the face of the PMT for a point-like target with no solenoidal field.

Estimates for the signal strength for 2 GeV electrons have been obtained for the point-like and extended targets with and without the 5 T solenoid field. Figures 70, 71, and 72 show angular distributions of the signal strength. The corresponding plots of the signal strength in the azimuthal angle range are shown in Figs. 73, 74, and 75. One can see that the signal strength increases with the polar angle. This is because the electrons scattered at a smaller angle travel a shorter distance in the radiator gas as compared to the electrons moving at larger angles. The minimum signal strength is estimated to be about 14-15 photoelectrons. For electrons scattered in the range of polar angles from  $5^\circ$  to  $35^\circ$  we have a complete and uniform coverage of the entire  $2\pi$  acceptance, as demonstrated by the azimuthal dependencies. The average signal strength is about 17 photoelectrons. This estimate has been obtained by taking into account the pos-

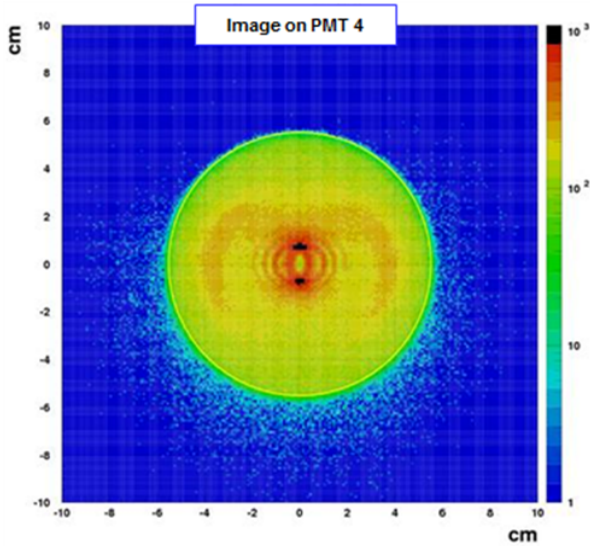


Fig. 67: Simulation result for the light collection pattern on the face of the PMT for a point-like target and a 5 T solenoidal field.

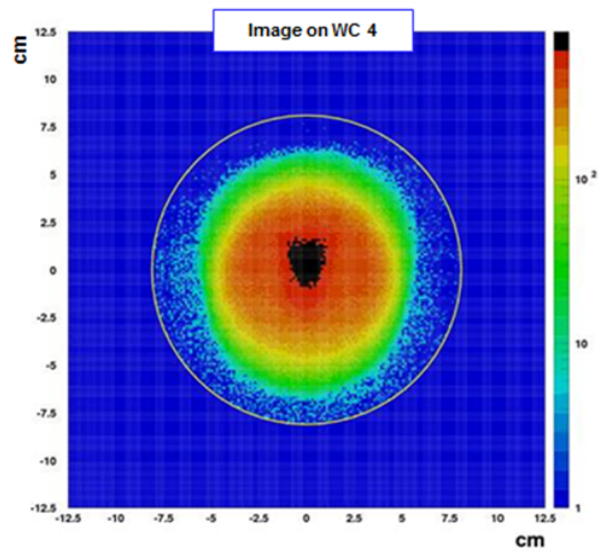


Fig. 69: Simulation result for the light collection pattern on the face of the Winston cone for a 10-cm-long target and a 5 T solenoidal field.

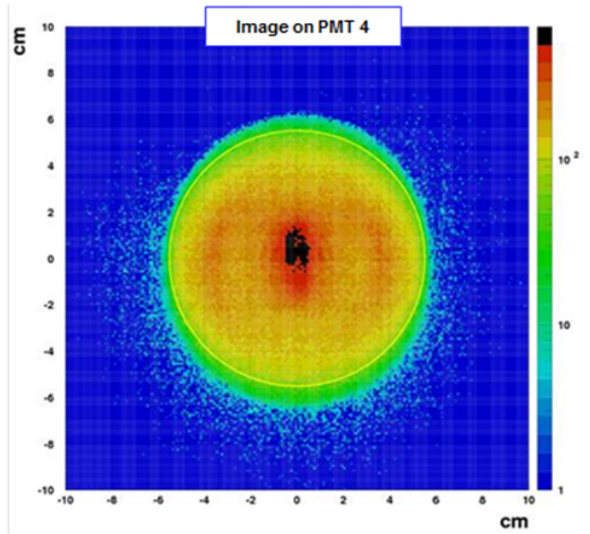


Fig. 68: Simulation result for the light collection pattern on the face of the PMT for a 10-cm-long target and 5 T solenoidal field.

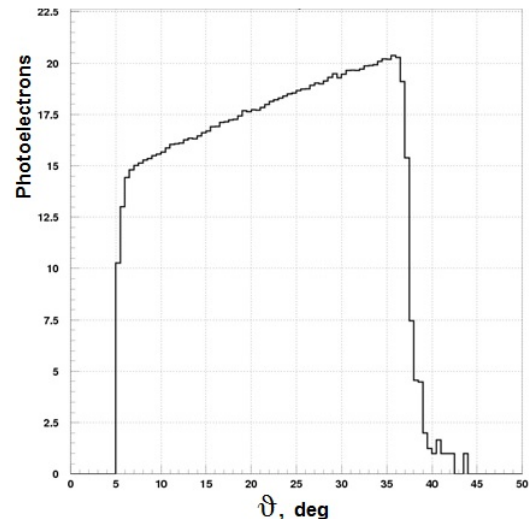


Fig. 70: Simulation results for the signal strength as a function of polar angle. Point-like target and no solenoidal field.

1355 sible reduction of the mirror reflectivity due to the  
 1360 unavoidable influence of the hard to control factors  
 1370 during the detector construction (dust and fume  
 deposition, mechanical imperfections of the reflective  
 surfaces, etc.) that were first observed during the  
 construction and maintenance of the CLAS Low  
 Threshold Cherenkov Counter [3].

One of sources of background events in the HTCC  
 is the secondary interactions of charged pions with

1365 components in the volume of the HTCC and with  
 1370 components outside the detector in the region  
 between the target and the HTCC entry window.  
 Charged pions with energies mostly below the de-  
 tection threshold can knock out relativistic  $\delta$  elec-  
 trons that generate Cherenkov light in the HTCC  
 volume. Some of that light can be focused by the  
 mirror on the PMTs. In our MC simulations we es-  
 timated the expected background rates. Of course

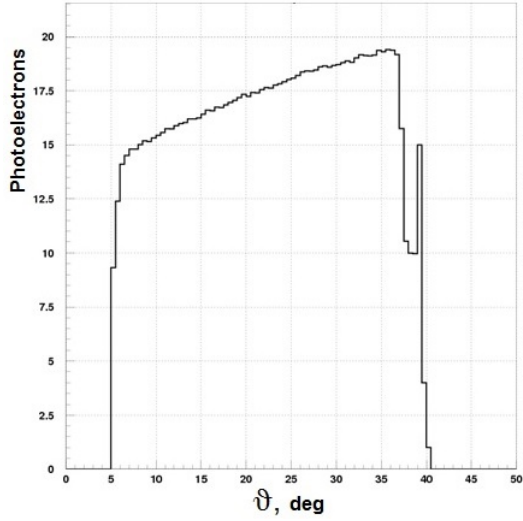


Fig. 71: Simulation results for the signal strength as a function of polar angle. Point-like target with a 5 T solenoidal field.

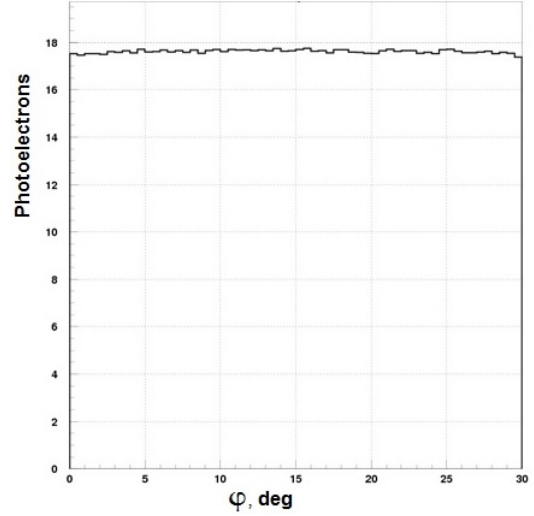


Fig. 73: Simulation results for the signal strength as a function of azimuthal angle. Point-like target with no solenoidal field.

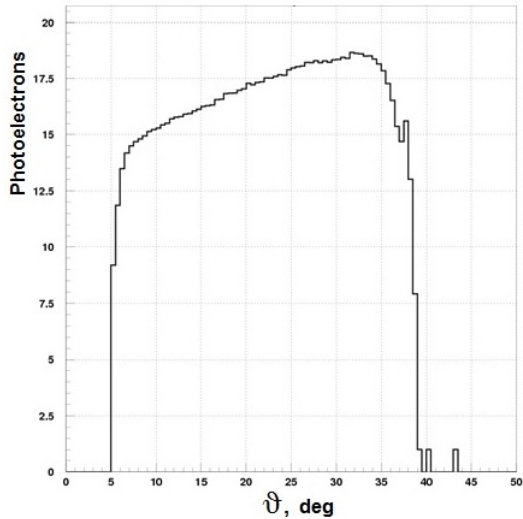


Fig. 72: Simulation results for the signal strength as a function of polar angle. 10-cm-long target with a 5 T solenoidal field.

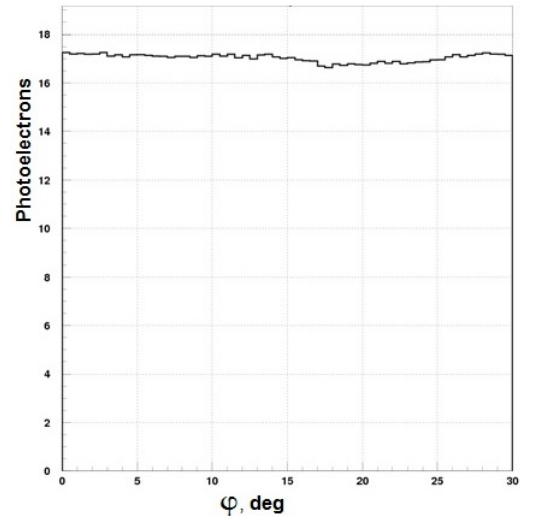


Fig. 74: Simulation results for the signal strength as a function of azimuthal angle. Point-like target with 5 T solenoidal field.

the rates depend on the actual thickness and distribution of the materials. We have specified in detail everything regarding the detector components in the simulation. With regard to outside components, we have taken into account the 10-cm-long cryogenic target filled with hydrogen, standard foam scattering chamber, and the air gap between the exit window of the chamber and the entry window of the HTCC. At the CLAS12 design luminosity of  $\approx 10^{35} \text{ cm}^{-2} \text{ s}^{-1}$ , the estimated total back-

ground rate for one half-sector is about 20 kHz.

The most important parameters for the HTCC are the electron detection efficiency and the charged pion rejection power. In Fig. 76 the simulation results on the rejection of charged pions are shown. Data are presented for four HTCC channels from one half-sector at three different thresholds of electron detection at 2 GeV: equivalent of 1, 2, and 3 photoelectrons. For the highest electron detection threshold ( $\geq 3$  photoelectrons) the estimated elec-

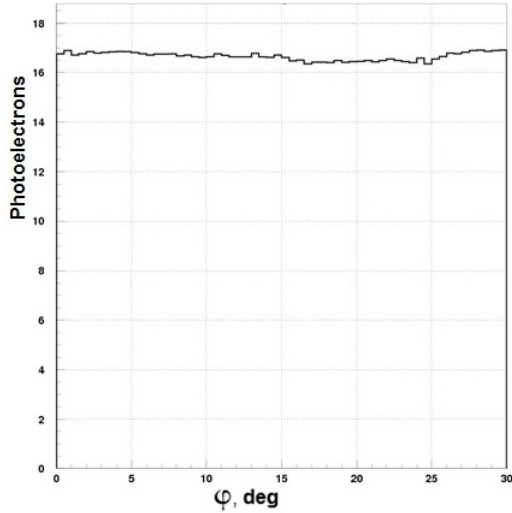


Fig. 75: Simulation results for the signal strength as a function of azimuthal angle. 10-cm-long target with 5 T solenoidal field.

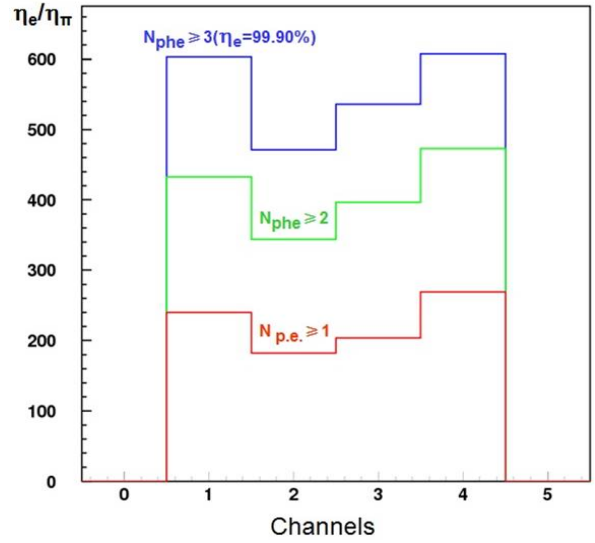


Fig. 77: Rejection of charged pions at 4 GeV from Monte Carlo studies.

tron detection efficiency is 99.9%. Similar results for 4 GeV electrons are shown in Fig. 77. One can conclude that at a threshold of 3 photoelectrons, the average rejection factor is greater than 1000 at 2 GeV and at least 500 at 4 GeV, with an electron detection efficiency close to 100%.

## 7. Performance

The HTCC is one of the major CLAS12 systems used in Hall B experiments with the electron beam. The most important aspects of the HTCC performance are that it provides good timing, high electron detection efficiency, and a high rejection factor for charged pions. Each of these parameters is critical for the quality of the data obtained in experiments since the detector, in combination with the forward electromagnetic calorimeter [12], provides a fast trigger signal for CLAS12. As shown in Section 6, the MC prediction for the HTCC detection efficiency for electrons is  $\approx 100\%$ . Figure 78 shows a distribution of the number of photoelectrons in the HTCC for elastically scattered 2 GeV electrons where the identification of a negative track as an electron was done based on kinematics. The corresponding thresholds applied were approximately 2.5 photoelectrons. The measurements were performed using a special procedure with a random trigger that was not correlated with the HTCC [6]. There were observed 27 events not detected by the HTCC due to the applied threshold. As shown, the electron detection efficiency is  $\eta = (99 \pm 0.2)\%$ , which is in good agreement with the MC estimate. This result can be considered as a conservative estimate due to the relatively high threshold used in the measurements.

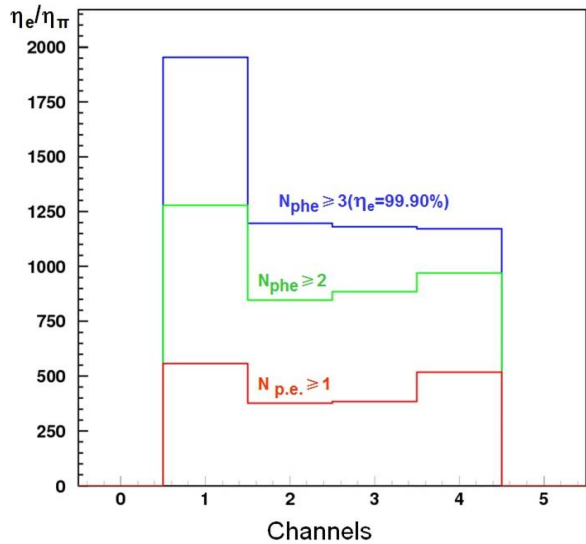


Fig. 76: Rejection of charged pions at 2 GeV from Monte Carlo studies.

1430 wider range of polar angles, where the average scattering  
 1435 angles are larger. Such electrons travel longer  
 distance in the radiator gas (by 10% to 30% depend-  
 ing on scattering angle). Consequently the signal  
 strength is higher for these electrons, and therefore  
 the detection efficiency is higher as compared with  
 the detection efficiency for elastically scattered elec-  
 trons.

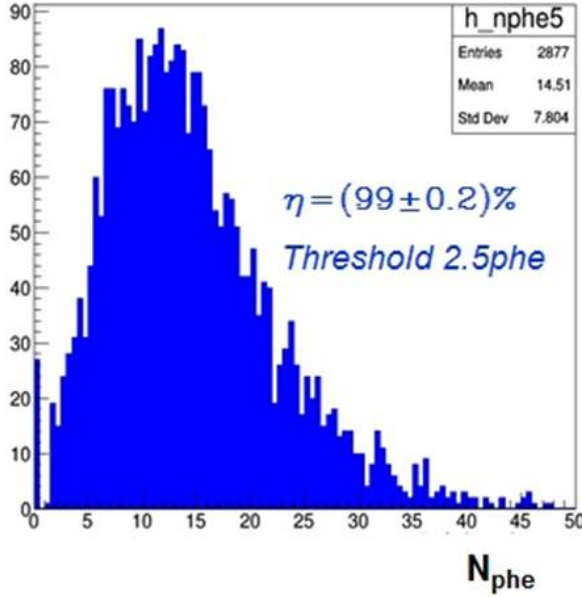


Fig. 78: Electron detection efficiency for elastically scattered electrons at 2 GeV. Data are obtained with the random trigger not correlated with the HTCC or other detector components of CLAS12.

Figure 79 shows the response of the detector over a wide range of particle momenta. The increase in the number of events at high momentum (>5 GeV) is due to registration of charged pions (above threshold for their registration in the HTCC) and this is clearly illustrated.

The signal strength in the HTCC depends on the actual properties of the mirror facets, such as their final shape and reflectance. The accuracy of the combined mirror assembly, the alignment of the HTCC components (mirror, PMTs, Winston cones), and the composition of the radiator gas, all influence the final results. The FADC histogram of the typical signal strength distribution obtained in half-sectors #1 and #2 of sector 1 is shown in Fig. 80. The signal strength for scattered electrons averaged over all HTCC channels is shown in Fig. 81. The experimentally measured mean value of 16.3 photoelectrons is close to the Monte Carlo

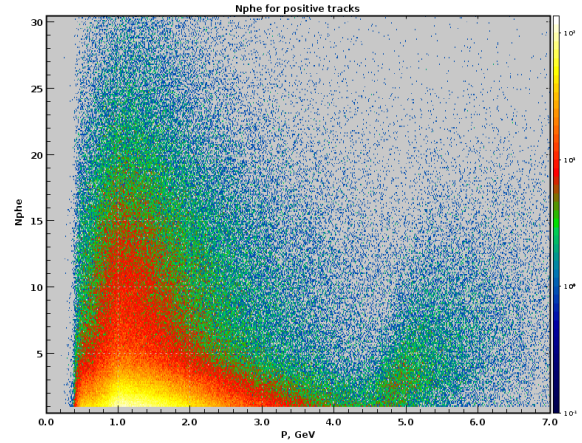


Fig. 79: Distribution of the HTCC response in terms of the number of photoelectrons vs. momentum over a wide momentum range, including the region beyond the threshold of charged pion registration (>5 GeV). The data were obtained for positrons and  $\pi^+$ -mesons.

simulation results (see Fig. 75).

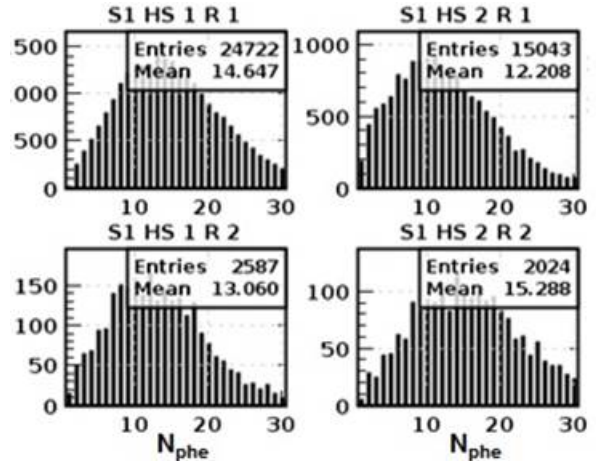


Fig. 80: Typical distributions of the signal strength in channels covering polar angles in the range of  $5^\circ$  to  $12.5^\circ$  (Ring 1) and  $12.5^\circ$  to  $20.0^\circ$  (Ring 2) within an azimuthal interval of  $60^\circ$ .

Figure 82 shows the uniformity of the HTCC response for different electron momenta. Fig. 83 shows the distribution of the HTCC response over the entire face of the mirror in the  $xy$  (transverse) plane.

The data show that the integrated signal strength is about 16.5 photoelectrons. At large electron polar scattering angles in range of  $27.5^\circ$  to  $35^\circ$ , the statistics are lower. Figure 84 shows the distribution of statistics in all 6 sectors.

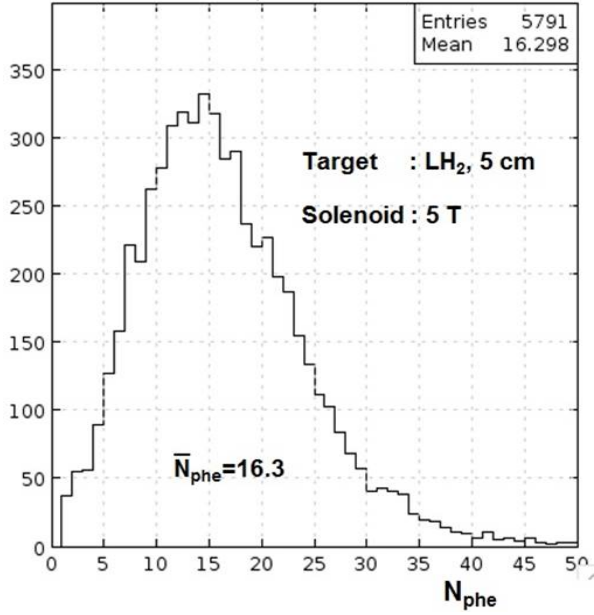


Fig. 81: The HTCC average signal strength for electrons from beam data at 10.6 GeV.

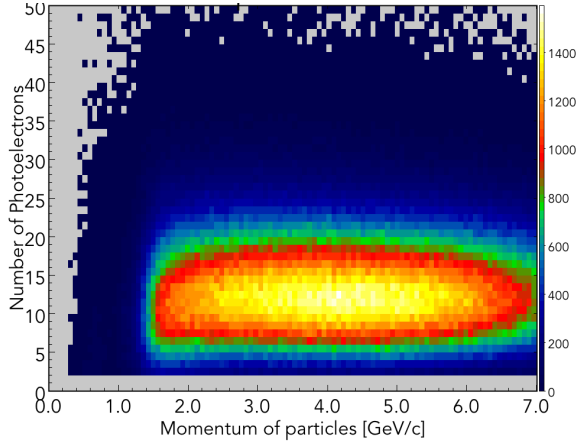


Fig. 82: The HTCC response for electrons: signal strength vs. momentum at 10.6 GeV electron beam energy.

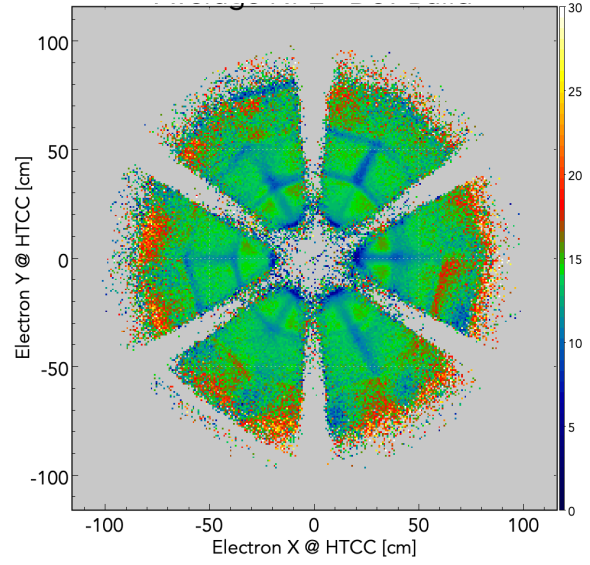


Fig. 83: The HTCC response (in terms of the number of photoelectrons) for electrons in the  $xy$ -plane of the mirror.

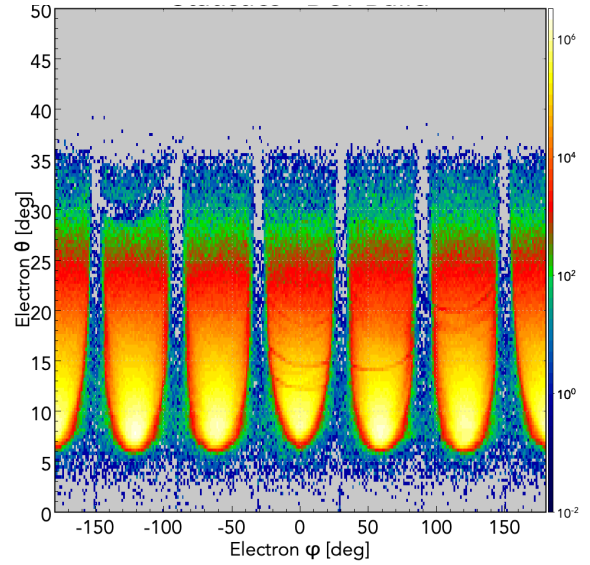


Fig. 84: Distribution of statistics in terms of electron polar angle vs. azimuthal angle in all 6 of the CLAS12 Forward Detector sectors.

We also note that in cases when the electrons cross a mirror close to its edges (at approximately at  $5^\circ$  and  $35^\circ$ ) one should expect unavoidable losses in the signal strength: some part of the Cherenkov light just passes by the mirror. As far as the internal borders between adjacent mirrors are concerned, there are similar losses that take place and are finally partially compensated due to the complete azimuthal symmetry of the detector, see Fig. 83. The width of the area along the internal boundaries that is deformed in the direction normal

to the mirror face due to the shrinkage of the glue is estimated to be between  $\sim 5 - 10$  mm. This area includes the technological zone of width  $\sim 0.5$  mm that does not reflect the light at all. As a result these regions (width up to  $\sim 10$  mm) along the internal boundaries between the mirror facets defuse the light impinging on the area, and therefore the signal strength is reduced. This edge effect is ex-

pected given the design of the detector.

## 8. Conclusions

The High Threshold Cherenkov Counter has been designed and built to meet all requirements that were defined mostly by its location and available space in front of the forward drift chambers of the CLAS12 spectrometer. A new technology of building lightweight multifocal ellipsoidal mirrors was developed and successfully used. The detector introduces a small amount of material in the CLAS12 acceptance that includes only the radiator gas and the mirror itself, which has thickness less than the total radiation length of the CO<sub>2</sub> radiator. There are no elements within the acceptance that support the HTCC mirror. The detector provides full azimuthal coverage and very efficient light collection: the Cherenkov light is detected after one reflection in 80% of events and after two reflections in the remaining 20% of events. Experiments with an electron beam have confirmed all design parameters of the detector. The performance of the HTCC is adequate, reliable, and meets all expectations for the CLAS12 experiments.

## 9. Acknowledgments

We appreciate the contribution and valuable help of D. McKay, C. Apeldoorn, and M. Powers in the development and implementation of a new technology for the HTCC construction. Only due to their direct involvement in the project and tight control of results was it possible to solve successfully so many difficult problems, and consequently completely avoid any compromises that would otherwise lead to reduced overall performance of the detector. This material is based upon work supported by the U.S. Department of Energy, Office of Science, Office of Nuclear Physics under contract DE-AC05-06OR23177.

## References

- [1] V. D. Burkert, et al., The CLAS12 Spectrometer at Jefferson Laboratory, to be published in Nucl. Inst. and Meth. A, (2020) (see this issue) (2020).
- [2] M. D. Mestayer, The CLAS12 Drift Chamber System, to be published in Nucl. Inst. and Meth. A, (2020) (see this issue) (2020).
- [3] G. Adams, et al., The CLAS Cherenkov detector, Nucl. Instrum. Meth. A465 (2001) 414–427. doi:10.1016/S0168-9002(00)01313-9.

- [4] N. Baltzell, et al., The CLAS12 Beamline and its Performance, to be published in Nucl. Inst. and Meth. A, (2020) (see this issue) (2020).
- [5] R. Fair, et al., The CLAS12 Superconducting Magnets, to be published in Nucl. Inst. and Meth. A, (2020) (see this issue) (2020).
- [6] B. Raydo, et al., The CLAS12 Trigger System, to be published in Nucl. Inst. and Meth. A, (2020) (see this issue) (2020).
- [7] S. Boyarinov, et al., The CLAS12 Data Acquisition System, to be published in Nucl. Inst. and Meth. A, (2020) (see this issue) (2020).
- [8] E. Bellamy, et al., Absolute Calibration and Monitoring of a Spectrometric Channel Using a Photomultiplier, Nucl. Instrum. Meth. A339 (1996) 468–476. doi:10.1016/0168-9002(94)90183-X.
- [9] P. Degtiarenko, Precision Analysis of the Photomultiplier Response to Ultra Low Signals, Nucl. Instrum. Meth. A872 (2017) 1–15. doi:10.1016/j.nima.2017.07.053.
- [10] V. Ziegler, et al., The CLAS12 Software Framework and Event Reconstruction, to be published in Nucl. Inst. and Meth. A, (2020) (see this issue) (2020).
- [11] M. Battaglieri, et al., The CLAS12 Forward Tagger, to be published in Nucl. Inst. and Meth. A, (2020) (see this issue) (2020).
- [12] G. Asryan, et al., The CLAS12 Pre-Shower Calorimeter, to be published in Nucl. Inst. and Meth. A, (2020) (see this issue) (2020).